

Change detection-based co-seismic landslide mapping through extended morphological profiles and ensemble strategy

Xin Wang^a, Xuanmei Fan^{a,*}, Qiang Xu^a, Peijun Du^b

^a State Key Laboratory of Geohazard Prevention and Geoenvironment Protection, Chengdu University of Technology, Chengdu 610059, China

^b School of Geography and Ocean Science, Nanjing University, Nanjing 210023, China

ARTICLE INFO

Keywords:

Co-seismic landslide mapping
Remote sensing
Change detection
Change vector analysis (CVA)
Extended morphological profiles (EMPs)
Multiple classifier ensemble

ABSTRACT

Co-seismic landslide mapping after earthquake event is essential for emergency rescue, geohazard prevention, and post-disaster reconstruction. Most co-seismic landslide mapping is primarily achieved via field surveys or visual interpretation of remote sensing images. However, such methods are highly labor-intensive and time-consuming, particularly over large areas. This paper proposed an automated co-seismic landslide mapping approach, which has three main advantages compared to state-of-the-art methods. First, it removes the dependence on the manual labeling for training samples through an unsupervised change detection process. Second, the approach takes the lead in introducing multi-scale extended morphological profiles to comprehensively describe the characteristics of various landslides induced by earthquake. Third, it is also the first attempt to employ ensemble strategy in landslide identification, which integrates the advantages of different machine learning-based classifiers, further improving the accuracy of recognition. Three experiments were carried out through multi-temporal Sentinel-2 and PlanetScope images acquired in China and Haiti. The results demonstrated the effectiveness and superiority of the proposed approach compared to other methods, providing an effective solution for complicated co-seismic landslide mapping task in the future.

1. Introduction

Geological hazards, which significantly endanger human live, infrastructures, and other property security, occur frequently worldwide (Cigna et al. 2012; Cigna et al. 2018). As a ubiquitous and typical geological hazard, landslides happen in terrestrial environments with slopes and become more frequent and harmful under the influence of global climate change, earthquake activity, and accelerated urbanization (Cui et al. 2019; Emberson et al. 2021; Huang and Fan 2013; Malamud et al. 2004; Schulz et al. 2009). Landslides induced by earthquakes are usually the ones with the largest severity of damage and the most serious losses (Huang et al. 2012; Valagussa et al. 2019). Therefore, a reliable inventory of co-seismic landslides after a strong earthquake event is crucial for timely quantitative hazard assessment, disaster relief, and subsequent risk governance, especially in mountainous regions with complex environment and inconvenient transportation (Chau et al. 2004; Galli et al. 2008). Furthermore, high-quality co-seismic landslide inventory is also meaningful for regional risk prevention and understanding the relationship between landslide patterns and seismic parameters (Chau et al. 2004; Gorum et al. 2011).

Earth observations from remote sensing images, which are provided with large area coverage but short revisit times, offer a great opportunity of monitoring land surface process in wide geographical areas compared to time and labor costly in-situ investigation. As the sensor technology developed in recent years, spectral, spatial, and temporal resolutions have been significantly improved simultaneously, giving an unprecedented chance to rapidly achieve landslide attribution and distribution induced by different triggering factors (Booth et al. 2013; Ciampalini et al. 2015). On this basis, many co-seismic landslide studies based on remote sensing technology have been carried out and developed.

The co-seismic landslide mapping algorithms can be broadly categorized into three types: manual interpretation-based, classification-based, and change detection-based methods (Metternicht et al. 2005; Zhong et al. 2020). Manual interpretation-based methods are the initial landslide detection ways since the remote sensing technology emerged. Images acquired from various sensors and sources, such as high-resolution satellite images, aerial photographs, and digital elevation models (DEMs) extracted from them, are utilized, along with the technological innovations of remote sensing in recent years. A series of characteristics derived from remote sensing images can be recognized

* Corresponding author.

E-mail address: fxm_cdut@qq.com (X. Fan).

<https://doi.org/10.1016/j.isprsjprs.2022.03.011>

Received 25 November 2021; Received in revised form 28 January 2022; Accepted 11 March 2022

Available online 19 March 2022

0924-2716/© 2022 International Society for Photogrammetry and Remote Sensing, Inc. (ISPRS). Published by Elsevier B.V. All rights reserved.

and used as the standards and references for interpretation (e.g., shape, size, photographic color, tone, mottling, texture, pattern, site topography, and setting), which have been widely adopted in many practical cases (Fiorucci et al. 2019; Fiorucci et al. 2011; Gao and Maro 2010; Guzzetti et al. 2012). However, their results are susceptible by subjective factors of different operators. More than that, it is time-consuming and labor-intensive to interpret landslides over a large area. Subsequently, classification-based methods were proposed, significantly improving the automation of landslide mapping process. With the continuous development of artificial intelligence algorithms, the classifiers enable to identify the characteristic difference between landslides and the other land covers through sufficient learning from training samples, realizing rapid and accurate recognition of landslides. Burrows et al. (2019) proposed a landslide classifier based on Synthetic Aperture Radar (SAR) coherence, which was estimated from the similarity in phase change between pixel ensembles, overcoming the variability of weather condition in co-seismic landslide mapping after the Gorkha earthquake in 2015. Kritikos et al. (2015) employed fuzzy logic and geographic information systems to establish the relationship between co-seismic slope failures and causative factors, which were derived from DEM, active fault map, and isoseismal data. The predictive capabilities of the models showed excellent performances in three historic landslide analysis. Object-based image analysis (OBIA) with different machine learning-based classifiers was also introduced for landslide mapping, greatly improving the results compared to pixel-based methods (Aksoy and Ercanoglu 2012; Amatya et al. 2021; Moosavi et al. 2014). Although classification-based approaches enhance the automation and accuracy of large-scale landslide mapping, not only co-seismic landslides are recognized, but also pre-event landslides are included. Hence, to identify co-seismic landslides individually, change detection-based techniques were proposed and proven more effective. The feasibility of the object-oriented change detection method has been verified in many cases of earthquake- and rainfall-induced landslides (Hölbling et al. 2015; Lu et al. 2011; Martha et al. 2012). Li et al. (2016) proposed a change detection-based Markov Random Field (CD-MRF) to achieve co-seismic landslides from multi-temporal aerial photographs. The advantages of convolutional neural network (CNN) in feature learning and target predicting were also adopted, and successfully applied in landslide mapping (Lei et al. 2019; Shi et al., 2021). Rather than optical image change detection, Niu et al. (2021) utilized multi-temporal SAR change detection to identify the landslides in the suburb of Shenzhen, China, providing a perspective in separating landslides from the changes caused by human anthropogenic. Change detection based on multi-temporal LiDAR has also been investigated for landslide recognition, which demonstrated superior results in heavily forested areas (Anders et al. 2013; Okyay et al. 2019). With the accumulation of open-source data, change detection-based landslide mapping have been successively developed on the remote sensing cloud computing platform (e.g., Google Earth Engine), providing effective means for the geological hazard identification in large areas (Scheip and Wegmann 2021; Yang et al. 2020).

Although the current co-seismic landslide mapping methods based on change detection have a high degree of accuracy and automation, the following shortcomings can benefit from additional improvements: 1) The existing pixel-based features often generate salt-and-pepper noise due to spectral anomalies and registration errors (Chen et al. 2012; Hussain et al. 2013; Walter 2004). OBIA is an effective way of dealing with this problem, but the selection of scale parameter is a tough issue. Though many methods related to scale optimization have been proposed, the optimal scale based on an evaluation (e.g., geometric or non-geometric metrics) is not always the best choice for a specific application (e.g., co-seismic landslide mapping) (Anders et al. 2011; Chen et al. 2018; Drăguț et al. 2014; Drăguț et al. 2010; Hossain and Chen 2019; Hu et al. 2021; Johnson and Xie 2011; Ming et al. 2015; Wang et al. 2019; Wang et al. 2021; Zhang et al. 2020); 2) Landslides usually occur in mountainous areas with complicated terrains, leading to certain

detection differences by various classifiers with sophisticated pixel value distribution in remote sensing images (Reichenbach et al. 2018; Zhong et al. 2020). Hence, an effective classifier for a study case may not be satisfactory to another research area (Shen et al. 2018; Woźniak et al. 2014); 3) Most methods of co-seismic landslide mapping are supervised or semi-supervised, relying on a learning process from the current or previous landslides (Guzzetti et al. 2012; Valkaniotis et al. 2018). However, labeling high quality landslide samples is a tedious work (Li et al. 2016). Additionally, the model trained from previous events may not be suitable for the current landslide recognition (Amatya et al. 2021).

In order to address the aforementioned problems, a novel automated co-seismic landslide mapping approach (Simplified as CD-EMPEs hereafter) is proposed. This approach utilizes differential multi-scale extended morphological profiles (EMPs) instead of object-based features to better characterize the spatial variance of landslides after earthquakes. Meanwhile, different machine learning-based classifiers are integrated to enhance the accuracy and robustness of the approach. In addition, to fully realize the automation, an unsupervised change detection method with multi-threshold segmentation is embedded, screening out co-seismic landslide pixels with highest reliabilities as training samples. Experimental results based on three real cases demonstrated the effectiveness and superiority of the proposed approach, proving its significant potential in co-seismic landslide mapping after earthquake events.

2. Study sites and datasets

Three earthquake-triggered landslides occurred respectively in Jiuzhaigou (Sichuan Province, China), Mainling (Tibet Autonomous Region, China), and the Departments of Grand'Anse and Sud, Haiti were considered in the research as shown in Fig. 1. The Jiuzhaigou area lies in the Songpan-Ganzi sub-block in the east of the Bayan Har block, which is in the middle section of the well-known North-South seismic zone in China (Fan et al. 2018). The Mainling area is located in Yarlung Tsangpo Grand Canyon, which represents a complex environment with the deepest gorge in the world (6 km), the largest water vapor channel on Tibetan Plateau, strong tectonic stress, and sensitive to climate change (Hu et al. 2019). The case study of Haiti earthquake-induced landslides is located in a mountainous area between Grand'Anse and Sud. Similar to the previous event in 2010, it occurred along the Enriquillo-Plantain Garden fault, an area where two tectonic plates grind against each other. The developed approach was tested in these three study areas for a comparative evaluation on the mapping performance.

2.1. Jiuzhaigou earthquake

An M_s 7.0 earthquake with a focal depth of 20 km occurred in Jiuzhaigou County, Sichuan Province, China at 21:19:46 (CST) on 8 August 2017. The coordinate of epicenter was 33.20°N 103.82°E. More than 1700 aftershocks occurred in the subsequent 36 h, resulting in 1883 landslides which removed vegetation and exposed many slopes (Fan et al. 2018). We selected a typical area free of cloud from the influenced area for the research, which is located in Zhangzha Town, the south of Jiuzhaigou, covering an area of 27.00 km². Two Sentinel-2 images of pre- and post-event were acquired on July 29 and September 7, 2017 from the European Space Agency's Sentinel Scientific Data Hub¹, respectively. The reflectance images of Top-of-atmosphere (Level-1C) were transformed to Bottom-Of-Atmosphere (Level-2A) through Sen2Cor plugin v2.9.0, which is available on the Sentinel Application Platform v8.0.0. Ten bands, including Blue, Green, Red, Vegetation Red Edge 1 to 3, NIR, Narrow NIR, and SWIR 1 to 2, were resampled to 10 m and combined in each temporal image. Table 1 summarizes the key

¹ Sentinel Scientific Data Hub: <https://scihub.copernicus.eu>.

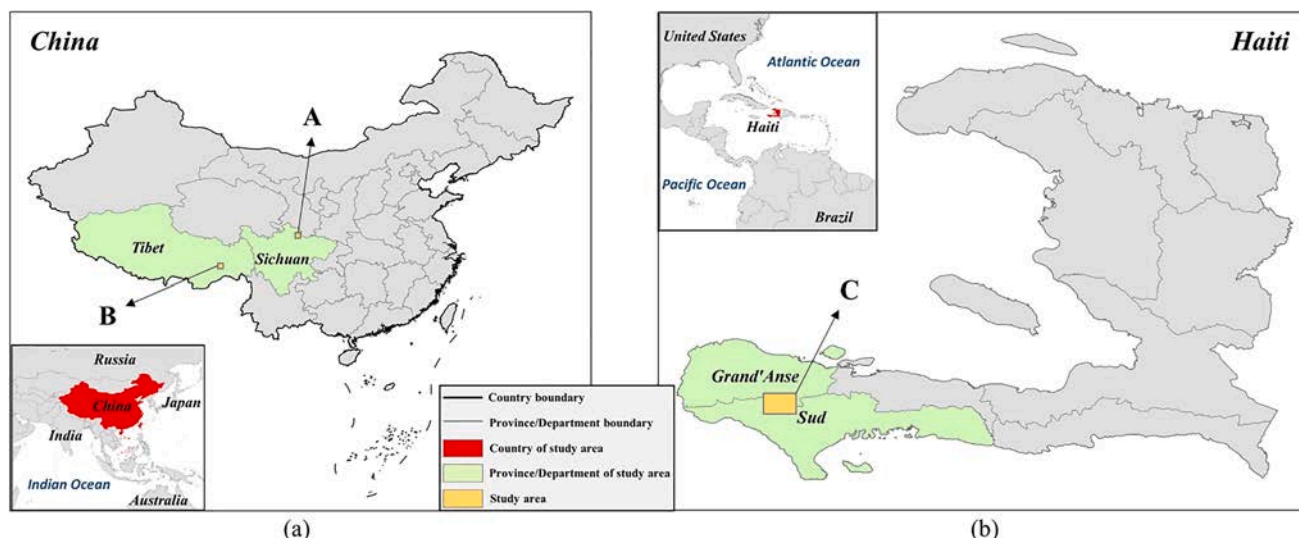


Fig. 1. Case studies for co-seismic landslide mapping. (a) A and B in the left are the locations of Jiuzhaigou and Mainling co-seismic landslides in China; (b) C in the right is the location of Haiti co-seismic landslides.

Table 1

Key parameters of the co-seismic landslide datasets.

Dataset	Jiuzhaigou, China	Mainling, China	Nippes, Haiti
Area	27.00 km ²	37.80 km ²	161.94 km ²
Image	Sentinel-2	PlanetScope	PlanetScope
Resolution	10 m (Resampled)	3 m	3 m
Bands	Blue (490 nm)	Blue (485 nm)	Blue (485 nm)
(Central wavelength)	Green (560 nm)	Green (545 nm)	Green (545 nm)
	Red (665 nm)	Red (630 nm)	Red (630 nm)
	Vegetation Red Edge 1 (705 nm)	/	/
	Vegetation Red Edge 2 (740 nm)	/	/
	Vegetation Red Edge 3 (783 nm)	/	/
	NIR (842 nm)	NIR (820 nm)	NIR (820 nm)
	Narrow NIR (865 nm)	/	/
	SWIR 1 (1610 nm)	/	/
	SWIR 2 (2190 nm)	/	/

information of the Jiuzhaigou dataset. To make a quantitative evaluation, the co-seismic landslides interpreted in our former work are used as references, in which a polygon-based interpretation was carried out through pre-earthquake SPOT-5 images (2.5 m) and post-earthquake Gaofen-1/2 images (1 m) as well as UAV photographs (0.2 m) (Fan et al. 2018). Fig. 2 shows the true color composite of pre- and post-event images, and the reference co-seismic landslide map.

2.2. Mainling earthquake

At 06:34 (CST) on 18 November 2017, an M_s 6.9 earthquake occurred in Mainling County, Tibet Autonomous Region, China, with the epicenter located at 29.87°N, 95.02°E and a focal depth of approximately 10 km, which is in the well-known stratigraphic suture zone and the Grand Canyon region of the Yarlung Zangbo River (Aitchison et al. 2000; Hu et al. 2020). 4395 seismic events occurred within 7 days after the event, triggering more than 1820 co-seismic landslides (Zhao et al. 2019). Two PlanetScope images were acquired on November 14 and December 19, 2017 from Planet Labs². A typical area free of cloud from

the influenced region was selected as the research area, which is located in the northeast of Mainling, covering 37.8 km² with 4 bands (Blue, Green, Red, and NIR) and a spatial resolution of 3 m. Table 1 summarizes the key information of Mainling dataset. The corresponding reference co-seismic landslide map for accuracy assessment was acquired based on (Hu et al. 2019), in which a polygon-based visual interpreting method was used to identify the co-seismic landslides in the proximity of the epicenter through high-resolution remote sensing images, including pre-earthquake satellite images from Landsat 7 ETM+ with 15 m resolution, Google Earth historical images, post-earthquake satellite images from SPOT 7 with 1.5 m resolution, and Sentinel-2 with 10 m resolution. Fig. 3 shows the true color composite of pre- and post-event images, as well as the reference co-seismic landslide map.

2.3. Haiti earthquake

At 08:29 (EDT) on 14 August 2021, an M_s 7.2 earthquake centered at 18.35°N, 73.45°W with a depth of 10 km struck the mountainous area of Nippes, Haiti. More than 900 aftershocks have been recorded in the following days (Martinez et al. 2021; Panuntun 2021). Combined with the heavy rainfall from Tropical Storm Grace on Aug. 16 and 17, a great many of landslides occurred, especially in the west steep mountainous areas, exposing many lives to danger. At least 2246 people were confirmed killed and above 12,763 people injured as of 29 November 2021, which is the worst disaster to Haiti since the 2010 earthquake (Haiti: Earthquake Situation Report No. 8 – Final. 2021³). To explore the detailed failures in the landslide area most severely affected by the earthquake, two 3 m-resolution PlanetScope images were acquired on August 10 and 29, 2021, which were the least cloud covered images closest to the dates of pre- and post-event, covering an area of 161.94 km² in approximately 57 km west of the epicenter. Table 1 summarizes the key information of Haiti dataset. United States Geological Survey (USGS) published the latest landslide point inventory for the Haiti earthquake on 7 December 2021, which included 4893 landslide points (Martinez et al. 2021). The inventory was produced by comparing mid-to high-resolution pre- and post-earthquake images, including Sentinel-2 (10 m resolution), WorldView (0.3–0.5 m resolution), Planet (2.7–4.0 m resolution), as well as a high-resolution (1.5 m resolution) Digital Elevation Model (DEM) that was derived from LiDAR collected from

² Planet Labs: <https://www.planet.com>.

³ <https://reliefweb.int/report/haiti/haiti-earthquake-situation-report-no-8-final-29-november-2021>.

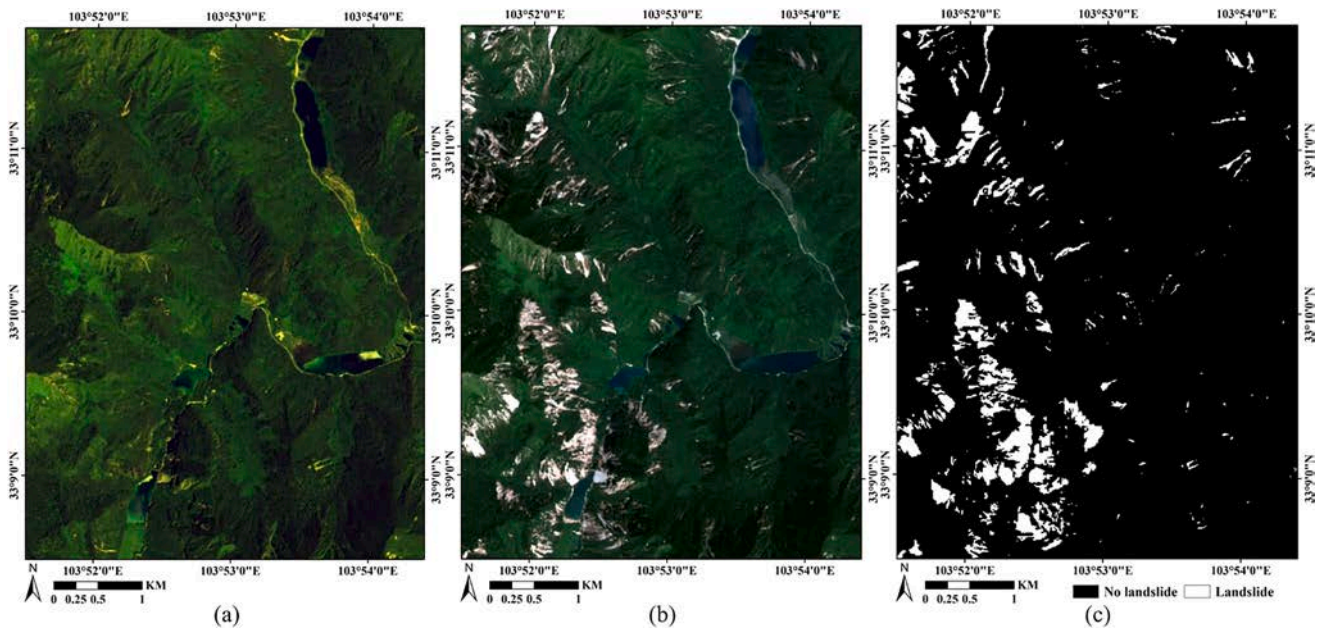


Fig. 2. The 10 m Sentinel-2 pre- and post-event images for Jiuzhaigou co-seismic landslide mapping. (a) Pre-event image; (b) Post-event image; (c) The reference map of co-seismic landslides, where black and white pixels represent no landslides and co-seismic landslides, respectively.

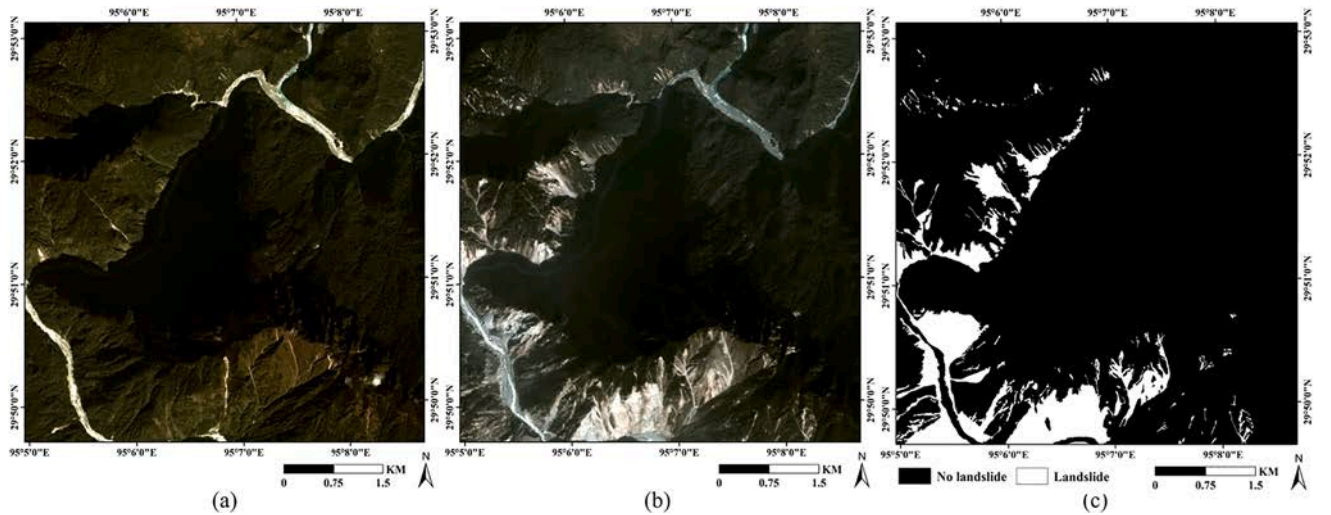


Fig. 3. The 3 m PlanetScope pre- and post-event images for Mainling co-seismic landslide mapping. (a) Pre-event image; (b) Post-event image; (c) The reference map of co-seismic landslides, where black and white pixels represent no landslides and co-seismic landslides, respectively.

2014 to 2016, to assure the landslides were associated with the earthquake. Taking the locations of these points as a reference, we performed a further polygon-based manual interpretation of co-seismic landslides in the study area via PlanetScope images before and after the earthquake. Fig. 4 shows the true color composite of pre- and post-event images.

3. Methodology

The proposed co-seismic landslide mapping approach mainly consists of three parts: 1) automated sample generation through multi-threshold change vector analysis (CVA), 2) EMPs extraction based on principal component analysis (PCA) and morphological filters, and 3) co-seismic landslide identification via multiple classifier ensemble. Fig. 5 displays the framework of the proposed approach.

3.1. Change vector analysis

CVA is a fundamental unsupervised change detection method, which achieves change information through pixel-wise radiometric comparison (Chen et al. 2003). Necessary image pre-processing, including radiometric calibration and geometric registration, needs to be implemented firstly to eliminate discrepancies between the multi-temporal remote sensing images. In the algorithm, a change vector is described through a magnitude and an angle of change from time 1 to time 2. Let the gray values of a pixel in time 1 and time 2 be $X = (x_1, x_2, \dots, x_l)^T$ and $Y = (y_1, y_2, \dots, y_l)$. The change vector can be defined as.

$$\Delta = Y - X = \begin{Bmatrix} y_1 - x_1 \\ y_2 - x_2 \\ \dots \\ y_l - x_l \end{Bmatrix} \quad (1)$$

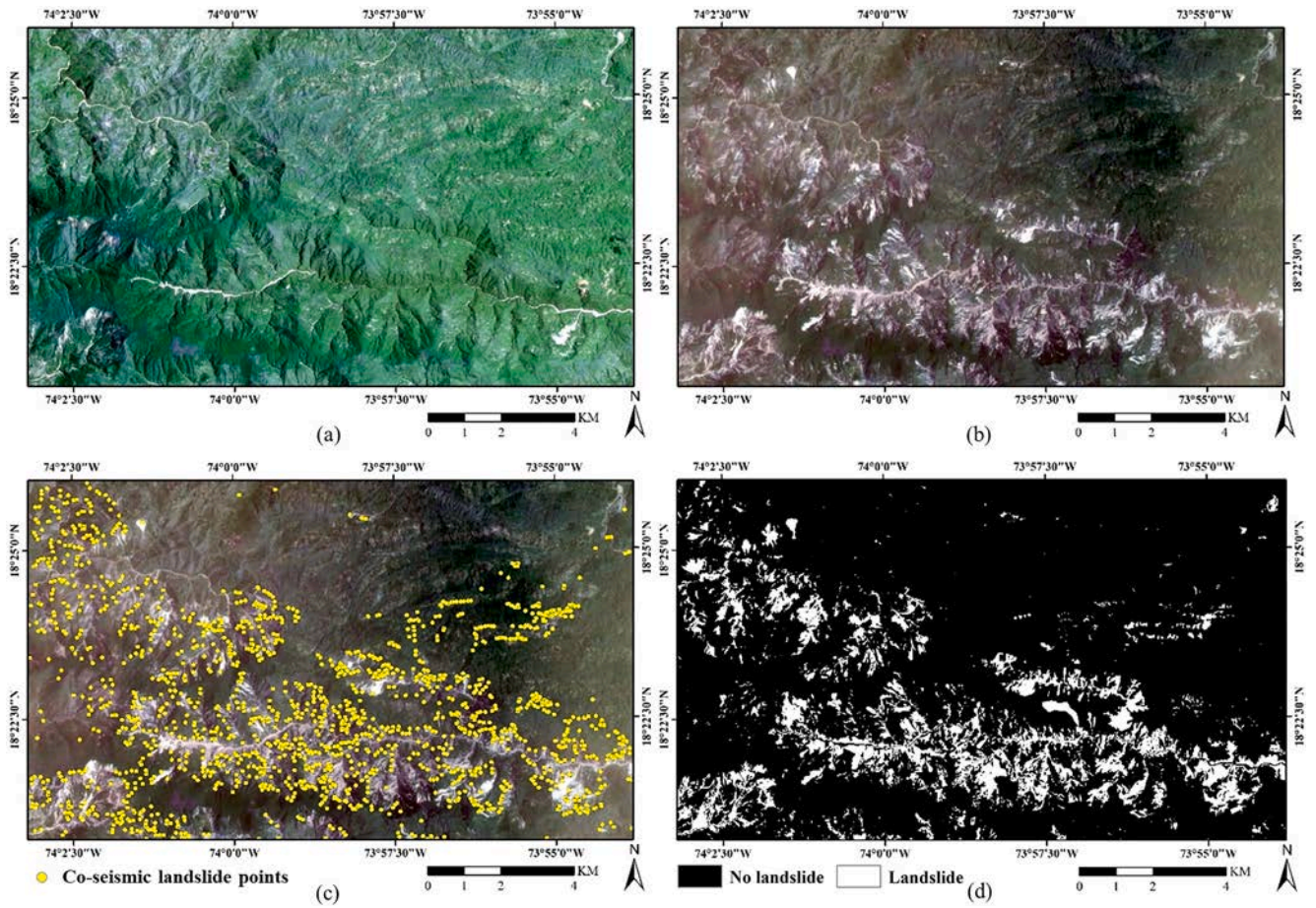


Fig. 4. The 3 m PlanetScope pre- and post-event images for Haiti co-seismic landslide mapping. (a) Pre-event image; (b) Post-event image; (c) Post-event image covered with co-seismic landslide points; (d) The reference map of co-seismic landslides, where black and white pixels represent no landslides and co-seismic landslides, respectively.

where l is the number of image bands. The magnitude of the change vector can be calculated through.

$$\|\Delta\| = \sqrt{(y_1 - x_1)^2 + (y_2 - x_2)^2 + \dots + (y_l - x_l)^2} \quad (2)$$

which represents the total difference between two images. The greater the $\|\Delta\|$, the higher the possibility of change. In general, if the magnitude of a change vector exceed a specific value, it is identified as a changed pixel. Otherwise, it is an unchanged pixel. However, if the boundary between changed and unchanged regions in change magnitude space is overlapped, it will be difficult to achieve a proper threshold for separating them. Therefore, the multi-level thresholding method should be introduced to make sure the definite changed and unchanged pixels, when the gray value distribution of magnitude image is not distinct. Otsu multi-level threshold method is an effective image segmentation technique having known the number of thresholds in advance (Otsu 1979). In the proposed approach, the optimal thresholds are considered to be the ones that maximize the between-class variances of three regions. Then, the landslide samples can be achieved as follows.

$$\|\Delta\| = \begin{cases} \text{landslide} & \|\Delta\| \geq T_{\text{landslide}} \\ \text{uncertain area} & T_{\text{no landslide}} < \|\Delta\| < T_{\text{landslide}} \\ \text{no landslide} & \|\Delta\| \leq T_{\text{no landslide}} \end{cases} \quad (3)$$

where $T_{\text{landslide}}$ and $T_{\text{no landslide}}$ are the magnitude thresholds to determine the lower limit of definite co-seismic landslide and upper limit of definite non-landslide pixels, respectively (Li et al. 2016; Lu et al. 2019; Lu et al. 2021). Consequently, these definite pixels can be utilized as

labeled samples, and the training samples can be directly selected from them for model training. This strategy is capable of both learning effective characteristics of co-seismic landslides and no landslides from accurate samples, while offering a good opportunity of completely automated identification process.

3.2. Extended morphological profiles

Earthquake-induced landslides vary in size and shape. The pixels of loose accumulations contain a variety of mixtures (e.g., vegetation, soil, and rocks), difficult to be easily distinguished with spectral information only. Considering the spatial relationship of pixels at different scales is capable of improving the recognition of co-seismic landslides. Morphological profile (MP) is an effective tool for extracting and reconstructing geometrical structures of objects in images. It has been successfully introduced in various remote sensing-based applications including land cover classification (Fauvel et al. 2008; Gu et al. 2016; Huang et al. 2016), target detection (Mongus et al. 2014; Valero et al. 2010; Zhao et al. 2020), and change detection (Hou et al. 2021; Liu et al. 2017; Volpi et al. 2013). This technique is based on two operators, erosion and dilation. The erosion operator shrinks the objects that are brighter than the surroundings, whereas the dilation operator expands them. Furthermore, the dilation of an eroded image is defined as opening, conversely, the erosion of a dilated operation is defined as closing (Benediktsson et al. 2005). The idea at the base of MP is to apply geodesic opening and closing transformations of increasing size to build a certain set of opening profiles (OPs) and closing profiles (CPs). The structuring element (SE), which is a template composed of a small

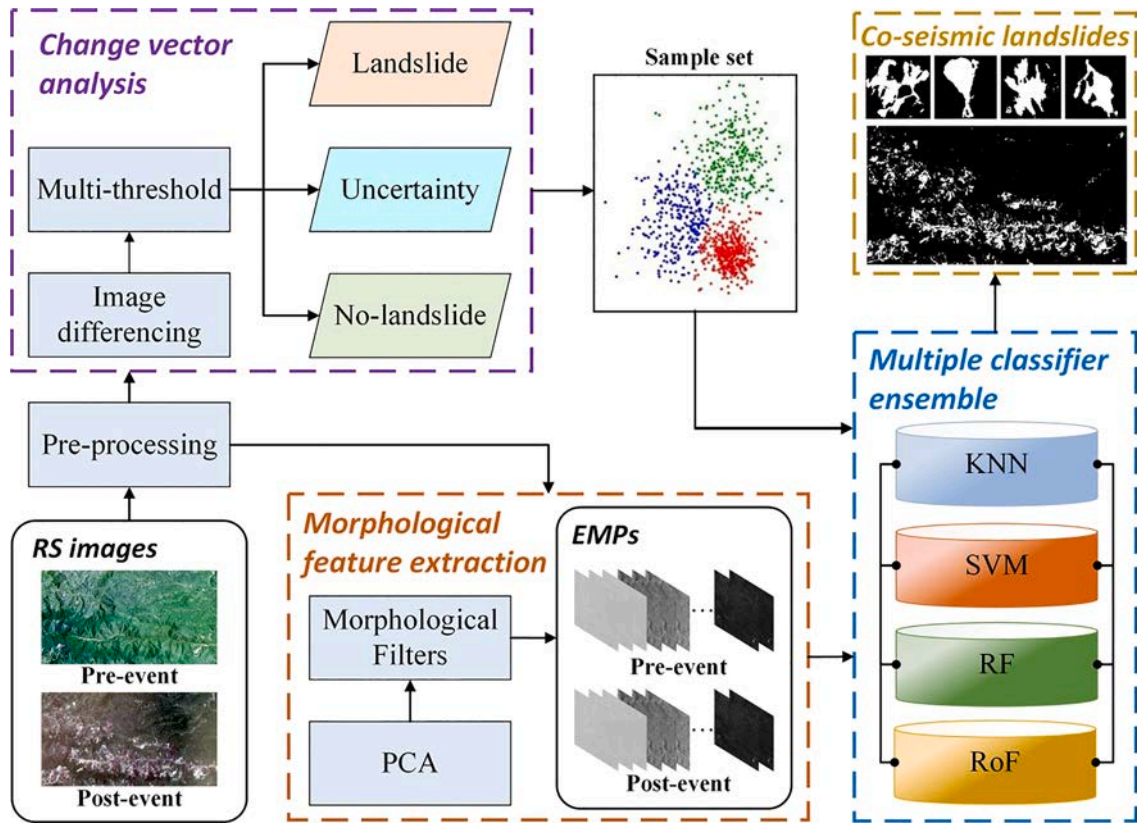


Fig. 5. Framework of the proposed approach. Note that KNN, SVM, RF, and RoF represent four machine learning methods of K-Nearest Neighbor, Support Vector Machine, Random Forest, and Rotation Forest, respectively.

matrix of pixels, provides the ability to specify the size and shape of MP. In detail, the matrix dimension, presented by a numeric value, specifies the size of the MP. The pattern of matrix specifies the shape of the MP. A benefit of this method is that an image can be reconstructed to extract the spatial information related to various sizes and shapes of objects through SEs with increasing scales and different patterns (Dalla Mura et al. 2011; Soille 2013). The opening by reconstruction (O_R) and closing by reconstruction (C_R) for a grayscale image are defined as:

$$O_R^i = R_\delta[\varepsilon^i(f)] \quad (4)$$

$$C_R^i = R_\varepsilon[\delta^i(f)] \quad (5)$$

where $\varepsilon^i(\cdot)$ and $\delta^i(\cdot)$ are the erosion and dilation operations with a SE of size i , while R_δ and R_ε are the geodesic reconstruction by dilation and erosion. Therefore, compared with the spectral information-based discrimination, the MPs provide the ability to fully excavate the spatial information in different scales and shapes for landslide identification.

The MPs derived from an original multi- or hyper-spectral remote sensing image (e.g., Sentinel-2, Hyperion) usually offer high dimensionality and information redundancy. More than that, considering the running time of feature extraction, model training, and target identification for large-scale imagery, it is inefficient when employing all of them in co-seismic landslide analysis (Lagrange et al. 2017). Hence, characteristic images need to be extracted in advance, the morphological operations (opening and closing) are then applied on each of them, yielding the features called EMPs (Benediktsson et al. 2005; Dalla Mura et al. 2011; Licciardi et al., 2012). PCA is a representative feature reduction method, which enables to reduce multi-variate domain of data into fewer dimensions (Abdi and Williams 2010). The features generated from the transformation, called principle components (PCs), account most variance of the data in the original feature space. In general, the

first few PCs which we considered contain approximately 99% of the total variance, aggregating most spectral and spatial information of the data (Licciardi et al. 2011). Therefore, EMPs, which are derived by morphological opening and closing on transformed PCs, can be adopted to better represent the spatial information as well as reduce the redundant information of MPs from original image bands, enhancing accuracy and computing efficiency (Gu et al. 2016). Let PC_k be the k th transformed PC, the EMPs can be achieved by applying a series morphological openings and closings operations using SEs with increasing sizes:

$$MP(PC_k) = \{O_R^m(PC_k), \dots, O_R^i(PC_k), \dots, O_R^1(PC_k), PC_k, C_R^1(PC_k), \dots, C_R^i(PC_k), \dots, C_R^m(PC_k)\} \quad (6)$$

where m is the number of SE scales implemented to each principle component. The extracted EMPs for each principle component contain $2m+1$ features, and the EMPs generated from n principle components of a single temporal image are displayed in formula (7). Following the previous notation, the EMPs of a single temporal image is a $n \times (2m+1)$ -dimensional vector. The final features for characterizing the co-seismic landslides information are produced by concatenating the bi-temporal EMPs, which has been proven to generate a complete map reproducing all of the changes that have occurred. As a result of this method, all of the available changes related to different sizes, which are reflected in the EMPs of different temporal images, enable to be preserved, guaranteeing that there is no loss of co-seismic information that may harm the identification process (Volpi et al. 2013; Zhang et al. 2018).

$$EMP(PCs) = \{MP(PC_1), MP(PC_2), \dots, MP(PC_n)\} \quad (7)$$

3.3. Multiple classifier ensemble

As long as definite labeled samples of co-seismic landslide targets and their characteristics are provided, it is possible to train a

comprehensive model to detect co-seismic landslides after an earthquake. Deep learning is currently a popular supervised recognition method that enable to predict targets via training samples. However, it usually requires a huge number of labeled samples. The sample records of historical earthquake events are not sufficient, and the earthquake environments are diverse from each other. Hence, deep learning-based landslide mapping is not able to balance accuracy and efficiency at current stage. Machine learning techniques are effective and efficient in dealing with target detection tasks with full consideration of various image characteristics. However, in the context of pattern recognition field, there is no guarantee that a specific classifier can always achieve the best performance in any condition (Chi et al. 2009), let alone identify co-seismic landslides via remote sensing images with complex topography influenced in mountainous areas. Therefore, four advanced machine learning-based classifiers, including K-Nearest Neighbor (KNN), Support Vector Machine (SVM), Random Forest (RF), and Rotation Forest (RoF), are adopted and integrated to enhance the co-seismic landslide recognition in this approach due to their relatively high accuracy, efficiency, and diversity. Their principles and advantages are as follows. 1) KNN is an instance-based learning algorithm that adopts the nearest distance in determining the category of a new vector in training data. During the training stage, the feature space is divided into multiple regions, and the training data are mapped into these regions according to the similarity of their contents. The unlabeled input data are categorized into a category through measuring the distance to each category. The simple implementation process of KNN makes it superior to other methods in the efficiency of co-seismic landslide identification. 2) SVM is selected thanks to its intrinsic robustness to high-dimensional data and ill-posed problems (Maulik and Chakraborty 2017). Its advantages of superior generalization ability and insensitive value are suitable for solving the change detection problems with small-size sample and nonlinear model (Mountrakis et al. 2011; Sheykhou et al. 2020). 3) RF is a non-parametric machine learning technique that enables to handle a great number of input features. It is conducted with a combination of a series of tree-structured classifiers, where the final result is subsequently achieved via selecting the output of the ensemble of tree-classifiers, yielding a better performance compared to single tree-classifier (Rodriguez-Galiano et al. 2012). RF usually does not require fine-tuning of parameters even when dealing with complex remote sensing scenarios, demonstrating excellent robustness and accuracy (Belgiu and Drăguț 2016). 4) RoF, whose principal aim is to encourage individual accuracy and diversity simultaneously, is developed from RF (Rodriguez et al. 2006; Xia et al. 2013). Compared to RF, it provides a new performing space though linear transformation to reconstruct feature subsets, which enhances the separability of image targets via decision tree training and improves the final classification performance (Du et al. 2015).

In the proposed ensemble scheme, we intend to integrate the advantages of all the techniques. Majority voting (MV) is implemented to elect the most frequent results for each pixel. For the case of a tie in MV, in which both landslide and no landslide are offered with equal votes, the result with the highest posterior probability is considered as the final outcome, as a higher posterior probability offers a higher reliability for a supervised result (Wang et al. 2020). With this method, the co-seismic landslide detection model can be described as follow.

$$C_{final} = \begin{cases} MV(C_1, C_2, C_3) & \text{if Not tie} \\ \max(C_1|X, C_2|X, C_3|X, C_4|X) & \text{if Tie} \end{cases} \quad (8)$$

where C_1, C_2, C_3 , and C_4 represent the change detection results via KNN, SVM, RF, and RoF, respectively. X and C_{final} represent all the possible classification results and the final classification result, respectively.

3.4. Comparative methods and parameter settings

To prove the effectiveness and superiority of the proposed approach,

four popular co-seismic landslide mapping approaches were conducted for comparison. First, conventional CVA, which can be used as a typical method for unsupervised and rapid landslide mapping, was implemented. The magnitude of difference image from time 1 to time 2 was separated by Otsu-based threshold to achieved co-seismic landslides. The second method integrated iterative principle component analysis and window recovery (ITPCA-WR). It was enabled to perform automatic radiometric normalization and mitigated side effects due to different acquisition conditions through iterative principal components. Besides, a post-processing procedure by filtering the pixels through a sliding window helped to address the misregistration in co-seismic landslide recognition (Falco et al. 2016). The size of sliding window was set as 3×3 in the subsequent experiments to obtain the optimal results. Third, an improved change detection-based Markov Random Field (CD-MRF) was carried out as is proposed in (Li et al. 2016), in which the spatial relationship of neighborhood pixels was preliminary taken into consideration. It is worth noting that the automated Otsu-based multi-threshold CVA was used firstly for candidate sample definition instead of manual tuning for fair comparison. The last comparative method was the open source SALaD system, which is a classification system based on OBIA and RF (Amatya et al. 2021). To improve the quality of landslide objects, we adopted the segmentation strategy proposed in (Martha et al. 2012). In detail, multi-resolution segmentation of post- and pre-event images were carried out, and multiple optimal scales were determined using plateau objective function (POF), respectively (Martha et al. 2011). Then, the main object level was created using the minimum optimal scale of the post-event image, whereas the sub-object level was created below the main object level using the minimum optimal scale of the pre-landslide image. The characteristics we extracted from the objects included spectral features (mean original bands, normalized difference vegetation index (NDVI), and brightness) and textural features (homogeneity, dissimilarity, contrast, standard deviation, entropy, second angular momentum, correlation, and mean derived from gray-level co-occurrence matrix (GLCM)). For the sake of fairness, multi-temporal stack images and random samples from the reference inventories were utilized and selected to train the RF models, and then applied to map co-seismic landslides.

In the proposed approach, to reduce the feature dimension while preserving the spatial information as much as possible, EMPs utilized the first three PCs from PCA in each temporal image. The SEs for EMPs extracted in Jiuzhaigou, Mainling, and Haiti co-seismic landslide mapping were set as [1,2], [2,3], and [2,3] with the shape of disk, respectively (Note that scale [p,q] represents the scales from p to q with a step of 1). The numbers of training samples in all the experiments (e.g., automated extraction from multi-threshold CVA in CD-MEF and CD-EMPES, and selecting from reference inventories in SALaD) were set as 500, where the numbers of landslide and non-landslide samples were both set to 250. The parameters of the classifiers adopted in the experiments (including the proposed and comparative methods) were set as follows. The number of nearest neighbors in KNN to find for classifying was set as 1. The type of kernel function used in SVM was Radial Basis Function (RBF), and the parameters (i.e., penalty parameter and Gamma) were selected based on the Particle Swarm Optimization (PSO) algorithm, a stochastic optimization technique to search the optimal parameters for SVM automatically (Melgani and Bazi 2008). For RF and RoF, trail-and-error was employed to identify a combination of constraining parameters that offered a good trade-off between model complexity and training validation performance. In detail, the number of decision trees in a model was set as 500. The number of attributes to each decision tree and the maximum decision tree depth were both set as 10. The experimental results of all the listed methods were achieved by the mean of 10 Monte Carlo runs to eliminate the random errors.

4. Results and analysis

4.1. Jiuzhaigou earthquake

The aforementioned methods were conducted and their performances were evaluated in Table 2, in which the best result of each index is shown in bold. It can be seen that CD-EMPES outperformed the other listed methods in terms of the highest overall accuracy (OA), which is 4.91%, 1.65%, 1.56%, and 1.13% higher than CVA, ITPCA-WR, CD-MRF, and SALaD, respectively. The Kappa coefficient that reflects the reliability of the result was also correspondingly higher by 0.2286, 0.1109, 0.1418, and 0.1378. From the perspective of detailed evaluation, CD-EMPES achieved the highest precision and F1-score with 74.87% and 0.7841. It also achieved second highest recall of 82.30%, only 1.97% lower than the highest recall. In summary, the proposed approach achieved the best performance in co-seismic landslide mapping.

The co-seismic landslide maps with different methods are displayed in Fig. 6, in which the following results can be noticed. The map produced by using CVA was discrete with more missed and false alarms, showing up in the form of salt-and-pepper noise, which was the main contribution to its worst accuracy. ITPCA-WR established a linear correlation model of the invariant areas before and after earthquake, which took subtle abnormal values of unchanged pixels into account, accurately identifying the pixel value shift caused by the earthquake induced landslides. More than that, the post-processing based on sliding window filtered out the noise caused by the registration error, improving the mapping accuracy. However, due to the influence of overall illumination and atmospheric difference between the dates of pre- and post-event, the lake in the northeast of the study area was mistakenly detected as newly-triggered landslides. Therefore, the reliability of ITPCA-WR was still insufficient. With consideration of both spectral and spatial information, CD-MRF further reduced missed and false detections result from spectral abnormalities and random distribution of loose substances produced by endogenic and exogenic geological processes during the geohazards. However, it led to some landslides discontinuous, leaving some obvious gaps and truncations. SALaD searched optimal segmentation scales considering the entire images and utilized the multiple object features to describe the change information, which mapped the landslides similar to real ground objects. In spite of this, the segmentation based on limited scales was difficult to fit the sizes of most landslides. Hence, under-segmentation led to some small-size landslides being ignored, whereas over-segmentation led to some blocky noise similar to pixel-based results. In comparison, CD-EMPES took multi-scale characteristics of landslides into account and fully learned the co-seismic landslide information before and after the earthquake, achieving more accurate recognition results in terms of size and shape.

To further explore the effectiveness of the proposed approach, three subsets of co-seismic landslide mapping were exemplified for illustration in Fig. 7, in which the red circles marked the obvious shortcomings. CVA produced obvious holes and noise in each scene. ITPCA-WR and CD-MRF could not fully recognize entire landslides in some cases, leaving the recognitions discontinuous and irregular. The mapping results of SALaD extremely relied on scale parameter and segmented objects. When an object was too large or small, it resulted in missed or false detections.

Table 2

Accuracy assessment of different co-seismic landslide mapping approaches on Jiuzhaigou dataset.

	CVA	ITPCA-WR	CD-MRF	SALaD	CD-EMPES
OA	92.22%	95.48%	95.57%	96.00%	97.13%
Kappa	0.5402	0.6579	0.6270	0.6310	0.7688
Precision	44.04%	61.52%	64.99%	72.73%	74.87%
Recall	84.27%	76.47%	65.15%	59.07%	82.30%
F1-score	0.5785	0.6819	0.6507	0.6519	0.7841

The subset result of the CD-EMPES achieved more accurate landslide information through visual interpretation and comparison.

4.2. Mainling earthquake

The proposed and comparative approaches were conducted for Mainling dataset. Their accuracies are listed in Table 3. As can be seen, the proposed approach achieved the highest OA of 97.26%, whereas the accuracies of ITPCA-WR, SALaD, CD-MRF, and CVA were 93.87%, 95.47%, 95.95% and 96.18%, respectively. To assess the quality of the results, CD-EMPES obtained the highest precision and F1-score with 93.44% and 0.8450. Meanwhile, it also achieved second best recall with 77.11%. In summary, combining the different evaluation indices listed, the proposed approach achieved the best performance among all the results.

The landslide maps derived from the aforementioned methods were displayed in Fig. 8. The CVA directly compared the spectral differences of multi-temporal images, leading to some salt-and-pepper noise, which might be caused by spectral anomalies or the movement of sporadic loose materials induced by the earthquake. Although ITPCA-WR identified landslides more continuous, apparent false detections were also generated. Identifying a long and narrow mountain road in the northeast of the study area as a co-seismic landslide was the most obvious one, which reflected the adverse impact of the spectral difference in invariant regions for ITPCA-WR. CD-MRF learned landslide information from reliable training samples and utilized post-processing considered spatial information, mitigating some noise and false detections. SALaD adopted object instead of pixel as processing unit to fill voids inside landslides, and reduced noise caused by spectral anomalies and registration errors. However, the shapes and sizes of earthquake-induced landslides were various. Though the optimal scales of pre- and post-event were searched respectively, it was difficult to take most landslide patterns into account. As a consequence, the landslides smaller than the scales could be ignored, whereas the landslides larger than the scales could be divided into multiple parts, increasing the probability of misclassification in the subsequent identification process. In contrast, CD-EMPES suppressed the interference of abnormal noise through multi-scale EMPs. Furthermore, it utilized the advantages of automatically obtained training samples and multiple advanced classifiers to comprehensively construct a co-seismic landslide model for the event and obtain the best recognition result.

Fig. 9 provides three subsets of landslide mapping in Mainling dataset. The red circles represent the errors in the results. In the first and second examples, it can be seen that some unchanged vegetations closed to landslides were easy to be falsely detected as landslides in CVA and ITPCA-WR. Some truncations and discontinuities existed in co-seismic landslide identification via ITPCA-WR and CD-MRF. SALaD reduced independent noise and obtained continuous landslide objects. However, a missed and false detection might occur when the shape of a segmented object did not exactly match the shape of the corresponding landslide. In contrast, CD-EMPES provided accurate recognitions in the first two scenes. For the third example with clouds in pre-event image and without cloud in post-event image, the clouds were falsely detected as co-seismic landslides in CVA, ITPCA-WR, and CD-MRF, while they were correctly identified as no landslides in SALaD and CD-EMPES thanks to object-based feature analysis and comprehensive modeling by multiple classifier ensemble, respectively.

4.3. Haiti earthquake

Since multi-temporal PlanetScope images were also obtained for Haiti co-seismic landslide mapping, the same scale parameters as Mainling dataset were employed in multi-scale EMP extraction to ensure the optimal performance. The accuracy assessments of the adopted methods are listed in Table 4. It can be seen that the proposed approach achieved the best performance among all the methods with the highest

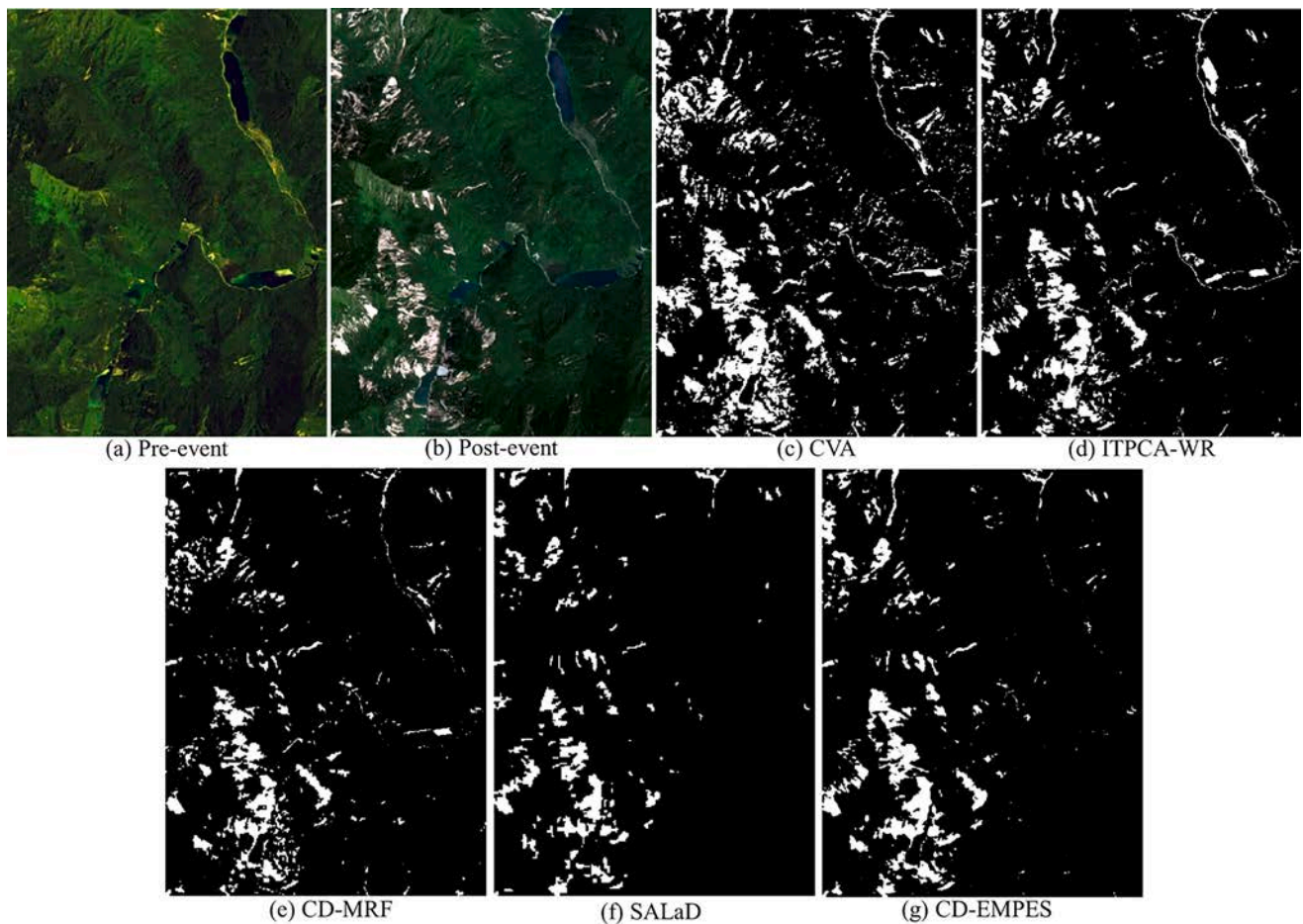


Fig. 6. Jiuzhaigou Sentinel-2 images of (a) pre-event and (b) post-event. Co-seismic landslide maps produced by (c) CVA, (d) ITPCA-WR, (e) CD-MRF, (f) SALaD, and (g) CD-EMPES, respectively.

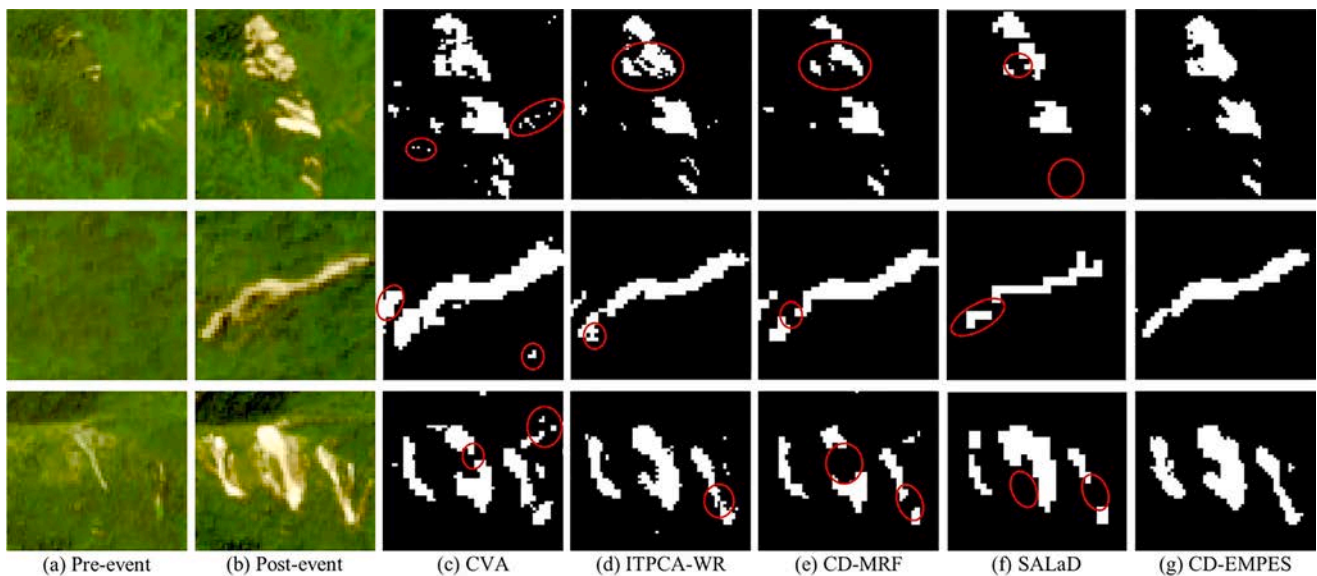


Fig. 7. Subset examples of co-seismic landslide maps in Jiuzhaigou dataset. (a) and (b) are the pre- and post-event images. (c) to (g) are the corresponding results derived from CVA, ITPCA-WR, CD-MRF, SALaD, and CD-EMPES, respectively.

OA (97.16%), Kappa coefficient (0.8617), Precision (97.03%), and F1-Score (0.8776). The overall performance was followed by SALaD. The metrics of SALaD were slightly inferior to CD-EMPES but the differences were not significant, indicating that the object-based hierarchical

segmentation effectively identified the shapes of landslides and separated co-seismic landslides from historical landslides simultaneously. The OAs of CD-MEF and CVA were similar. However, CD-MRF obtained a higher precision but a lower recall than CVA. In fact, CVA resulted in

Table 3
Accuracy assessment of different co-seismic landslide mapping approaches on Mainling dataset.

	CVA	ITPCA-WR	CD-MRF	SALaD	CD-EMPES
OA	96.18%	93.87%	95.95%	95.47%	97.26%
Kappa	0.7872	0.6674	0.7344	0.7151	0.8301
Precision	78.50%	66.33%	90.89%	83.27%	93.44%
Recall	83.33%	74.42%	64.67%	66.52%	77.11%
F1-score	0.8084	0.7014	0.7557	0.7396	0.8450

Table 4
Accuracy assessment of different co-seismic landslide mapping approaches on Haiti dataset.

	CVA	ITPCA-WR	CD-MRF	SALaD	CD-EMPES
OA	94.38%	87.93%	95.09%	95.28%	97.16%
Kappa	0.7713	0.5014	0.7432	0.7768%	0.8617
Precision	72.38%	52.11%	95.48%	85.42%	97.03%
Recall	90.31%	63.13%	64.44%	75.84%	80.11%
F1-score	0.8036	0.5709	0.7695	0.8035	0.8776

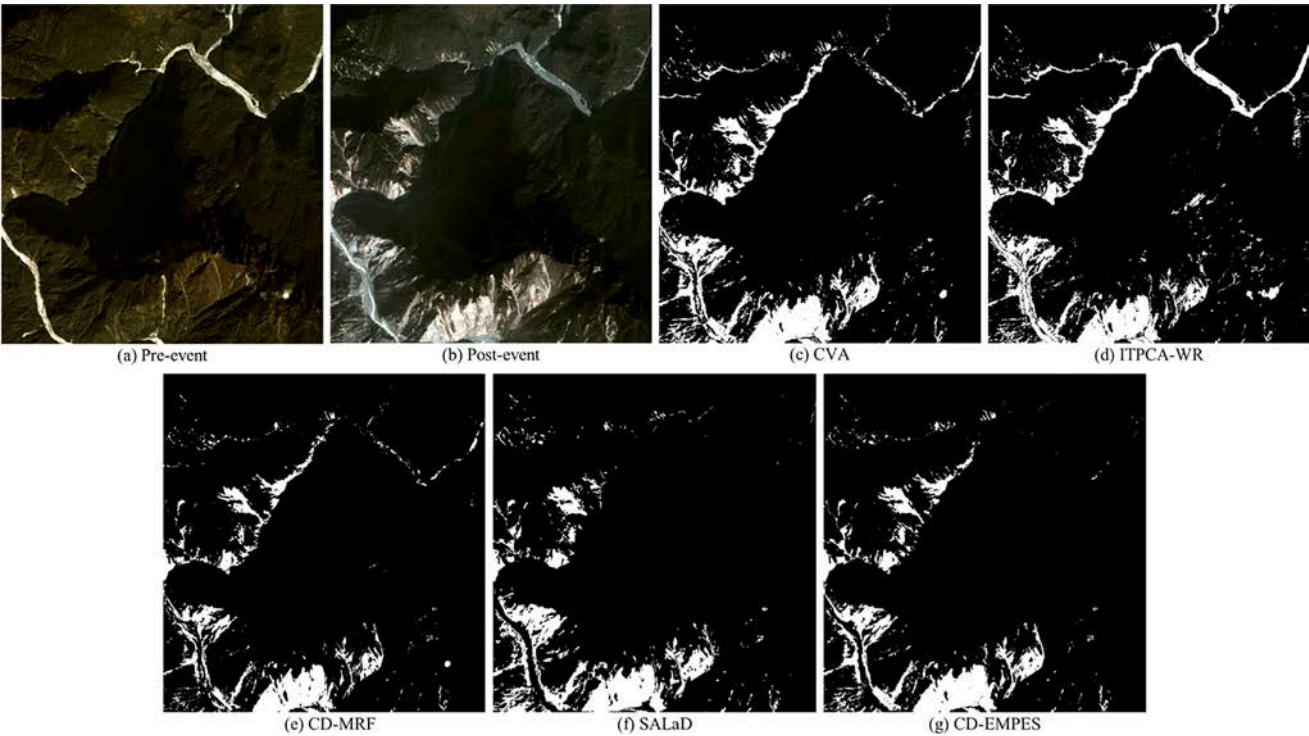


Fig. 8. Mainling PlanetScope images of (a) pre-event and (b) post-event. Co-seismic landslide maps produced by (c) CVA, (d) ITPCA-WR, (e) CD-MRF, (f) SALaD, and (g) CD-EMPES, respectively.

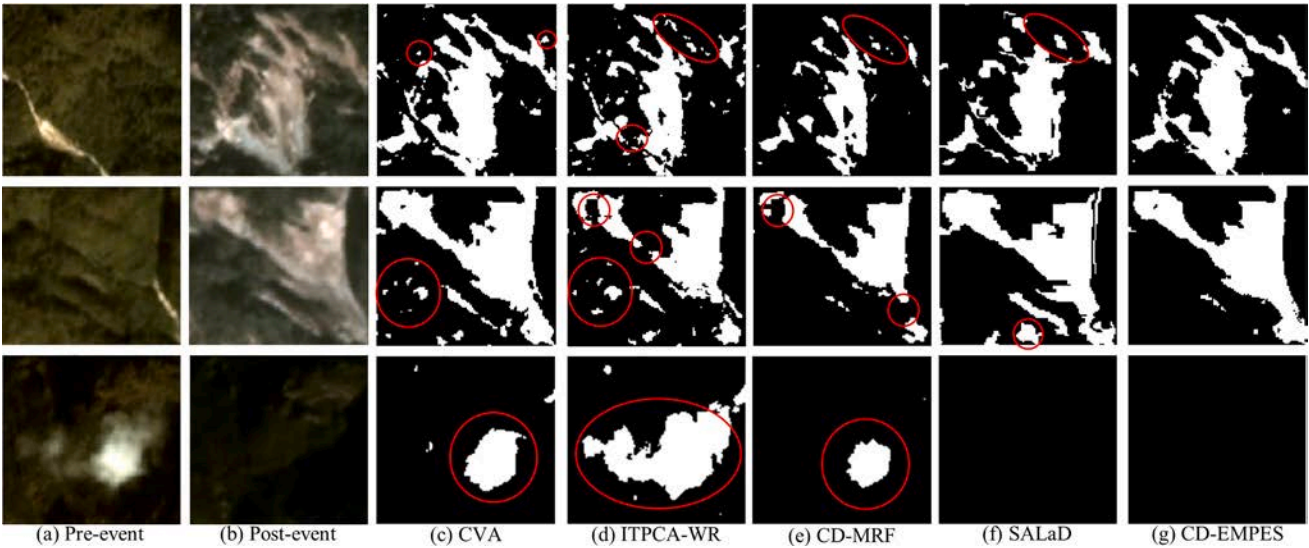


Fig. 9. Subset examples of co-seismic landslide maps in Mainling dataset. (a) and (b) are the pre- and post-event images. (c) to (g) are the corresponding results derived from CVA, ITPCA-WR, CD-MRF, SALaD, and CD-EMPES, respectively.

more false detections via difference image segmentation, in which more no landslides or historical landslides were identified as co-seismic landslides. The CD-MRF considered the spatial relationship of surrounding pixels, leading to an improvement of correct rate in identified co-seismic landslides. Nonetheless, some obvious co-seismic landslides were missed. ITPCA-WR obtained the worst performance in this case, whose metrics were much lower than other methods.

Figs. 10 and 11 display the entire and subsets of co-seismic landslide maps produced by the different methods. It can be observed from the figures that CVA achieved more false detections, whereas CD-MRF achieved more missed detections. However, ITPCA-WR has the problems in false and missed detection at the same, which resulted from the spectral difference in invariant regions. SALaD took the object as the processing unit, and performed better than the above methods in outlining the shapes and boundaries of co-seismic landslides. CD-EMPES took multi-scale characteristics of co-seismic landslides into account, achieving the results most consistent with the reality.

4.4. Parameter sensitivity

4.4.1. Scale parameters

SE scales are the key parameters of EMPs, which directly determine the sizes of the newly-triggered landslides considered in the proposed approach. To evaluate the detailed influences, CD-EMPES was carried out in different datasets with various SE scales considered, including [1], [2], [3], [4], [1,2], [2,3], [3,4], [1,3], [2,4], and [1,4]. The results are displayed in Fig. 12. It can be concluded that the SE scales of EMPs had a certain impact on the final results. For the Sentinel-2 (10 m resolution) Jiuzhaigou dataset, the best mapping performance was based on the SE scales of [1,2]. However, for PlanetScope (3 m resolution) Mainling and Haiti datasets, the highest accuracy was acquired with the scales of [2,3]. This indicates that a good condition for feature level fusion can be

reached by integrating the information represented in certain adjacent scales, whereas combining more scales information cannot always guarantee an increase in mapping accuracy. In addition, the optimal scale parameters to obtain the best result can be affected by the spatial resolution of remote sensing images. For the recognition of co-seismic landslides, small-scale EMPs are conducive to target identification in medium- and high-resolution images, whereas appropriately increasing the SE scales can achieve better performances in high- and very high-resolution images.

4.4.2. Training samples

The number of training samples input usually has an impact for a supervised classifier. For exploring its detailed influence on the performance of CD-EMPES, different numbers of training samples selected from multi-threshold based CVA were tested in the Jiuzhaigou, Mainling and Haiti events. Fig. 13 shows the OAs under the condition of different training sample numbers. The results revealed a significant increase in OA when the numbers of training samples were less than or equal to 100 (Jiuzhaigou and Haiti datasets) or 300 (Mainling dataset), whereas they tended to stabilized afterward. Therefore, selecting a proper amount of the automatically extracted co-seismic landslide labels as training samples can achieve a result with considerable accuracy.

5. Discussion

5.1. Sample extraction

Automated sample extraction is a crucial step to achieve full automation in the proposed approach. Landslide and non-landslide samples can be separated by using segmentation for intensity pixels of difference image. Otsu-based CVA was carried out for sample extraction. To improve the accuracy of the selected samples, a multi-threshold

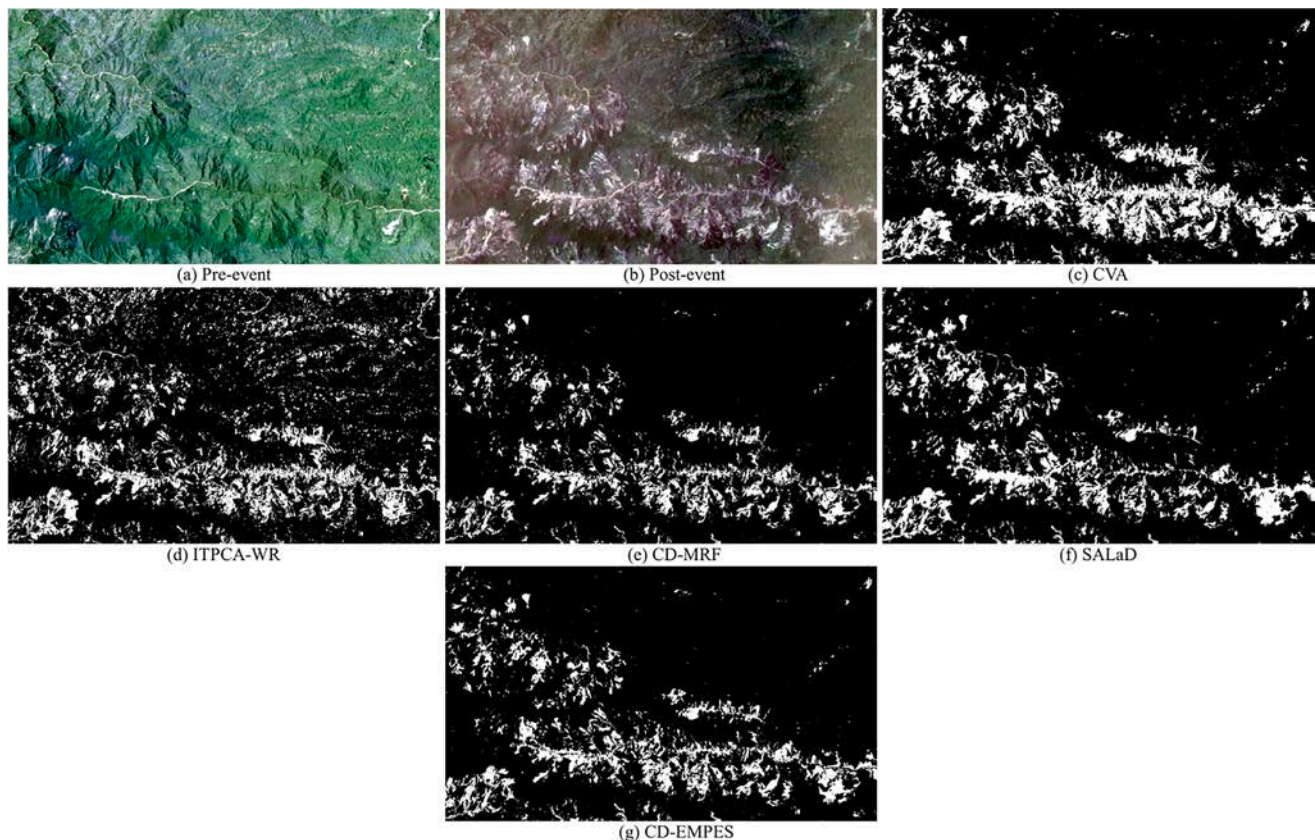


Fig. 10. Haiti PlanetScope images of (a) pre-event and (b) post-event. Co-seismic landslide maps produced by (c) CVA, (d) ITPCA-WR, (e) CD-MRF, (f) SALaD, and (g) CD-EMPES, respectively.

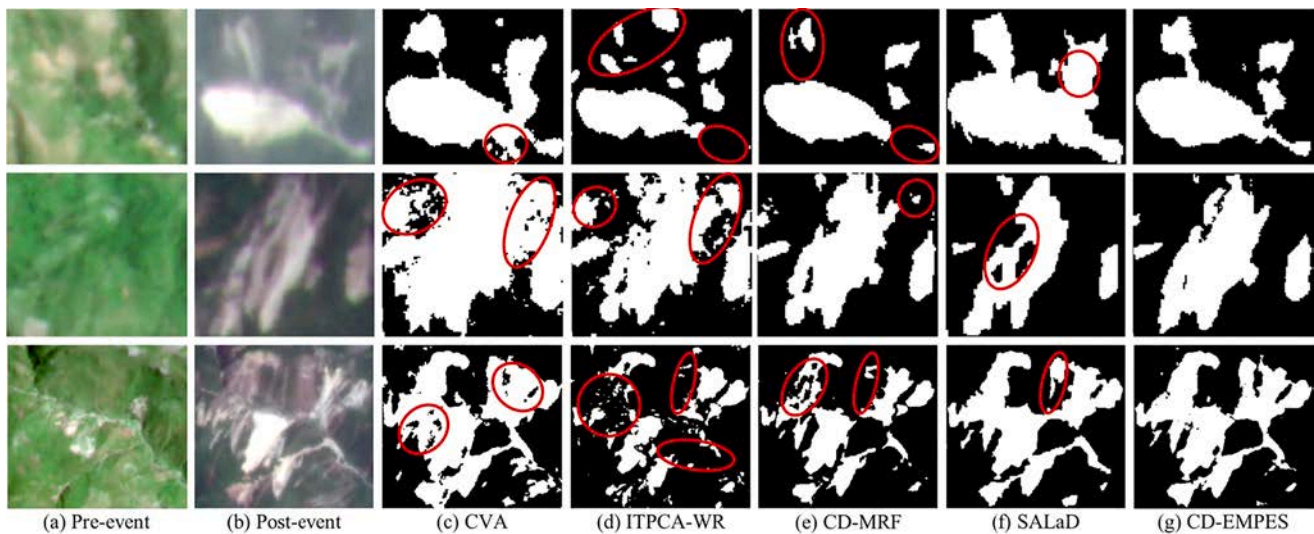


Fig. 11. Subset examples of co-seismic landslide maps in Haiti dataset. (a) and (b) are the pre- and post-event images. (c) to (g) are the corresponding results derived from CVA, ITPCA-WR, CD-MRF, SALaD, and CD-EMPES, respectively.

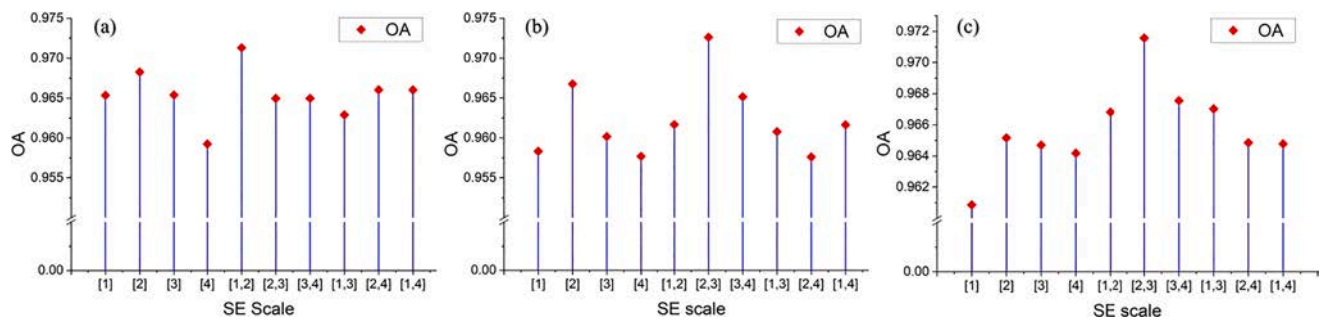


Fig. 12. Scale analysis of EMPs for (a) Jiuzhaigou dataset, (b) Mainling dataset, and (c) Haiti dataset in the proposed CD-EMPES approach.

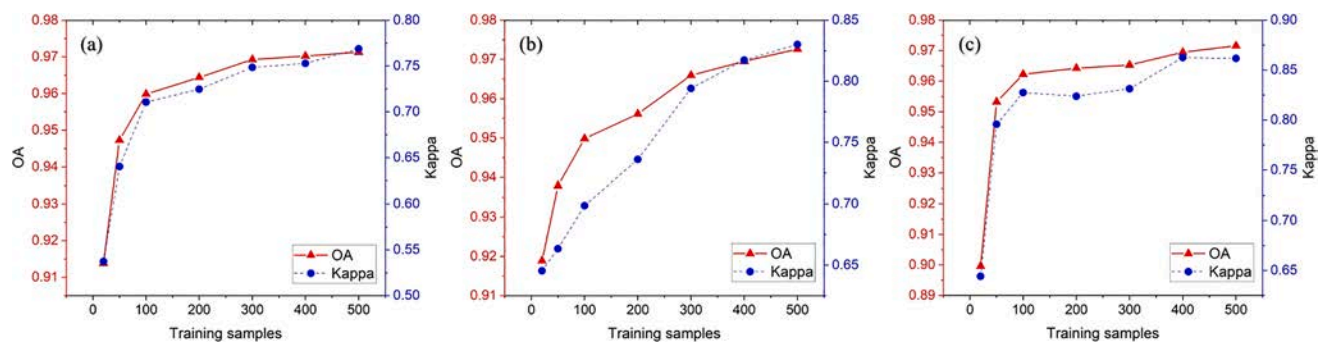


Fig. 13. OAs and Kappa coefficients of (a) Jiuzhaigou dataset, (b) Mainling dataset, and (c) Haiti dataset in the proposed CD-EMPES approach with different numbers of training samples.

segmentation rather than single-threshold segmentation was conducted in the proposed approach. Fig. 14 illustrates the correctness of the single and multiple threshold-based sample extractions in Jiuzhaigou dataset, Mainling dataset, and Haiti dataset. Although the sample numbers decreased by multiple thresholds compared to single thresholds, the correct rates of landslide samples increased notably from 44.04%, 78.50%, and 72.38% to 67.39%, 92.47%, and 96.02% in Jiuzhaigou dataset, Mainling dataset, and Haiti dataset, respectively. More than that, the correct rates of non-landslide samples increased further from 98.87%, 98.20%, and 98.53% to 99.58%, 99.59%, and 99.39% in Jiuzhaigou dataset, Mainling dataset, and Haiti dataset, respectively. Therefore, multi-threshold segmentation significantly improved the

accuracy and reliability of the training samples for co-seismic landslide mapping, providing a good basis for the subsequent model training and predicting.

5.2. Ensemble strategy

The ensemble strategy is also a key part of the proposed approach to ensure the accuracy and robustness of co-seismic landslide mapping. To explore the importance of ensemble strategy for intelligent landslide identification, each base classifier was used for recognition separately, in which the other settings were the same with the proposed CD-EMPES. Their performances in Jiuzhaigou, Mainling, and Haiti events are

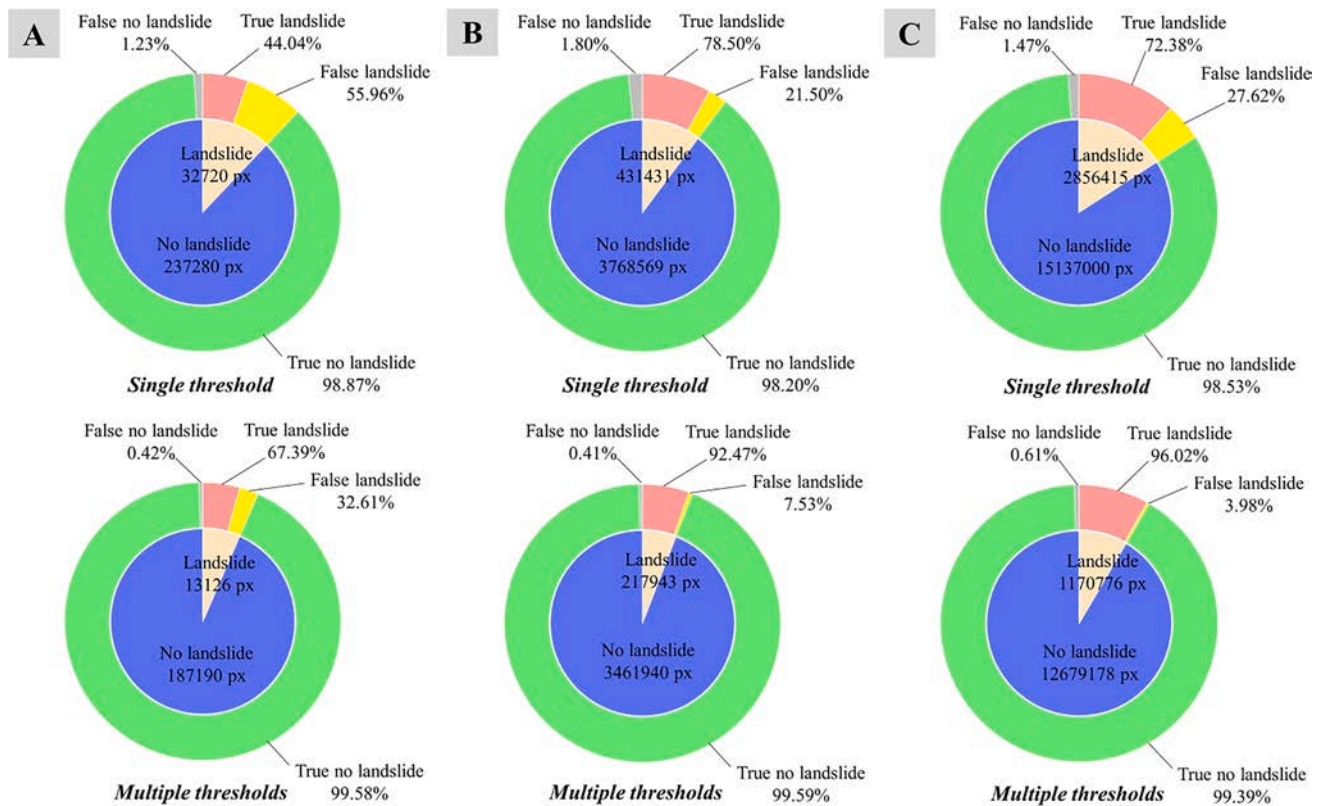


Fig. 14. Correctness of automatic sample extractions with single threshold and multiple thresholds in (A) Jiuzhaigou dataset, (B) Mainling dataset, and (C) Haiti dataset.

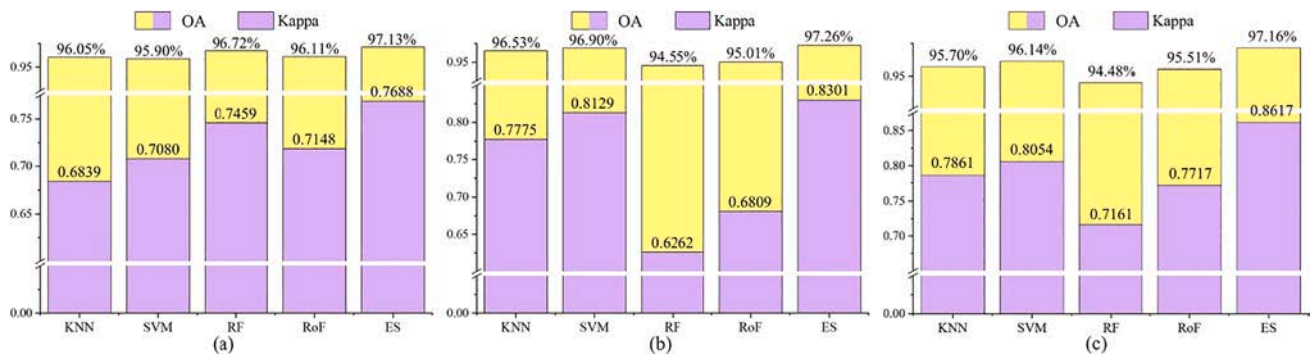


Fig. 15. OAs and Kappa coefficients of different classifiers in (a) Jiuzhaigou dataset, (b) Mainling dataset, and (c) Haiti dataset.

displayed in Fig. 15. The orders of landslide mapping performances of the four independent classifiers were not consistent in different datasets. The accuracy and Kappa of independent classifiers from high to low were RF, RoF, SVM, and KNN in Jiuzhaigou dataset, whereas the orders of these indices were SVM, KNN, RoF, and RF in Mainling and Haiti datasets, revealing the sensitivity of machine learning-based classifiers to pixel value distribution of remote sensing images in complex environments. The advantage of ensemble strategy was comprehensively considering and integrating the results of multiple classifiers in any scenario, notably enhancing the accuracy, reliability and robustness. In view of this, CD-EMPES was capable of achieving the highest OA and Kappa coefficient in each dataset.

6. Conclusion

A novel approach CD-EMPES was proposed in this paper to address the complex co-seismic landslide mapping problem automatically and

accurately. Compared to the existing methods, the main contributions of CD-EMPES are summarized as follows. First, this approach adopts the multi-threshold CVA to obtain the training samples for mapping, which not only removes the dependence on landslide information via manual labeling, but also avoids the influence of pre-earthquake landslides. Second, CD-EMPES is the first attempt to employ EMPs in landslide interpretation, in which multi-scale EMPs not only take the spatial relationship between adjacent pixels into account, but also consider the scale characteristics of landslides, significantly improving the identification accuracy. Third, CD-EMPES utilizes ensemble strategy in landslide recognition for the first time. By combining the algorithm advantages of different advanced classifiers, the optimal mapping outcome can be achieved through fully learning effective information from the obtained samples. Given its effectiveness and accuracy, the proposed co-seismic landslide mapping approach has great potential to be applied in rapid response and emergency management of natural hazards.

Note that CD-EMPES is generally more applicable to co-seismic landslides rather than rainfall-induced landslides. Compared to co-seismic landslides, rainfall-induced landslides are mostly shallow and clustered, resulting in small image spectral variations and strong recovery ability (Iwahashi et al. 2012; Zhang et al. 2019). In addition, under the support of the lubricating and homogenizing process of precipitation on land surface, the spectral difference between landslide and no landslide was reduced. These factors will harm the process of automatic sample extraction based on multi-threshold CVA embedded in CD-EMPES, subsequently affecting the final mapping performance. Additionally, rainfall-induced landslides are usually accompanied by debris flows, fluctuations of water levels, and other changes (Lin et al. 2004; Shen et al. 2021). Further separation is often required for the changed samples extracted in the early step or the landslide results identified in the later step. Combined with the above reasons, the performance of CD-EMPES in rainfall-induced landslides is not as good as that of co-seismic landslides. We will further explore a more generalized approach based on this study to make it applicable for landslide mapping with different triggering factors.

Declaration of Competing Interest

The authors declare that they have no known competing financial interests or personal relationships that could have appeared to influence the work reported in this paper.

Acknowledgements

This research was supported by the Funds for Creative Research Groups of China (Grant No. 41521002). The authors would like to thank Dr. Wei Zhang from Nanjing University for his assistance in manual interpretation of Haiti co-seismic landslides. The authors would like to thank Matthew Senyshen from Queen's University for his advice to improve the presentation of the manuscript. The authors would also like to thank the associate editor who handled their article and the anonymous reviewers for providing truly insightful comments and suggestions that are significantly helpful to improve the quality of the manuscript.

References

- Abdi, H., Williams, L.J., 2010. Principal component analysis. *Wiley Interdiscip. Rev. Comput. Stat.* 2 (4), 433–459.
- Aitchison, J.C., Badengzhu, Davis, A.M., Liu, J., Luo, H., Malpas, J.G., McDermid, I.R.C., Wu, H., Zlabrev, S.V., Zhou, M.-F., 2000. Remnants of a Cretaceous intra-oceanic subduction system within the Yarlung-Zangbo suture (southern Tibet). *Earth Planet. Sci. Lett.* 183 (1–2), 231–244.
- Aksoy, B., Ercanoglu, M., 2012. Landslide identification and classification by object-based image analysis and fuzzy logic: An example from the Azdavay region (Kastamonu, Turkey). *Comput. Geosci.* 38 (1), 87–98.
- Amatya, P., Kirschbaum, D., Stanley, T., Tanyas, H., 2021. Landslide mapping using object-based image analysis and open source tools. *Eng. Geol.* 282, 106000. <https://doi.org/10.1016/j.enggeo.2021.106000>.
- Anders, N.S., Seijmonsbergen, A.C., Bouten, W., 2013. Geomorphological change detection using object-based feature extraction from multi-temporal LiDAR data. *IEEE Geosci. Remote Sens. Lett.* 10 (6), 1587–1591.
- Anders, N.S., Seijmonsbergen, A.C., Bouten, W., 2011. Segmentation optimization and stratified object-based analysis for semi-automated geomorphological mapping. *Remote Sens. Environ.* 115 (12), 2976–2985.
- Belgiu, M., Drăguț, L., 2016. Random forest in remote sensing: A review of applications and future directions. *ISPRS J. Photogramm. Remote Sens.* 114, 24–31.
- Benediktsson, J.A., Palmason, J.A., Sveinsson, J.R., 2005. Classification of hyperspectral data from urban areas based on extended morphological profiles. *IEEE Trans. Geosci. Remote Sens.* 43 (3), 480–491.
- Booth, A.M., Lamb, M.P., Avouac, J.-P., Delacourt, C., 2013. Landslide velocity, thickness, and rheology from remote sensing: La Clapière landslide, France. *Geophys. Res. Lett.* 40 (16), 4299–4304.
- Burrows, K., Walters, R.J., Milledge, D., Spaans, K., Densmore, A.L., 2019. A new method for large-scale landslide classification from satellite radar. *Remote Sensing* 11 (3), 237. <https://doi.org/10.3390/rs11030237>.
- Chau, K.T., Sze, Y.L., Fung, M.K., Wong, W.Y., Fong, E.L., Chan, L.C.P., 2004. Landslide hazard analysis for Hong Kong using landslide inventory and GIS. *Comput. Geosci.* 30 (4), 429–443.
- Chen, G., Hay, G.J., Carvalho, L.M.T., Wulder, M.A., 2012. Object-based change detection. *Int. J. Remote Sens.* 33 (14), 4434–4457.
- Chen, G., Weng, Q., Hay, G.J., He, Y., 2018. Geographic object-based image analysis (GEOBIA): Emerging trends and future opportunities. *GIScience & Remote Sensing* 55 (2), 159–182.
- Chen, J., Gong, P., He, C., Pu, R., Shi, P., 2003. Land-use/land-cover change detection using improved change-vector analysis. *Photogramm. Eng. Remote Sens.* 69 (4), 369–379.
- Chi, M., Kun, Q., Benediktsson, J.A., Feng, R., 2009. Ensemble classification algorithm for hyperspectral remote sensing data. *IEEE Geosci. Remote Sens. Lett.* 6, 762–766.
- Ciampalini, A., Raspini, F., Bianchini, S., Frodella, W., Bardi, F., Lagomarsino, D., Di Traglia, F., Moretti, S., Proietti, C., Pagliara, P., Onori, R., Corazza, A., Duro, A., Basile, G., Casagli, N., 2015. Remote sensing as tool for development of landslide databases: the case of the Messina Province (Italy) geodatabase. *Geomorphology* 249, 103–118.
- Cigna, F., Osmanoglu, B., Cabral-Cano, E., Dixon, T.H., Ávila-Olivera, J.A., Garduño-Monroy, V.H., DeMets, C., Wdowinski, S., 2012. Monitoring land subsidence and its induced geological hazard with Synthetic Aperture Radar Interferometry: A case study in Morelia, Mexico. *Remote Sens. Environ.* 117, 146–161.
- Cigna, F., Tapete, D., Lee, K., 2018. Geological hazards in the UNESCO World Heritage sites of the UK: From the global to the local scale perspective. *Earth Sci. Rev.* 176, 166–194.
- Cui, Y., Cheng, D., Choi, C.E., Jin, W., Lei, Y., Kargel, J.S., 2019. The cost of rapid and haphazard urbanization: lessons learned from the Freetown landslide disaster. *Landslides* 16 (6), 1167–1176.
- Dalla Mura, M., Benediktsson, J.A., Chanussot, J., & Bruzzone, L. (2011). The Evolution of the Morphological Profile: from Panchromatic to Hyperspectral Images. In S. Prasad, L.M. Bruce, & J. Chanussot (Eds.), *Optical Remote Sensing: Advances in Signal Processing and Exploitation Techniques* (pp. 123–146). Berlin, Heidelberg: Springer Berlin Heidelberg. https://doi.org/10.1007/978-3-642-14212-3_8.
- Drăguț, L., Csillik, O., Eisank, C., Tiede, D., 2014. Automated parameterisation for multi-scale image segmentation on multiple layers. *ISPRS J. Photogramm. Remote Sens.* 88, 119–127.
- Drăguț, L., Tiede, D., Levick, S.R., 2010. ESP: a tool to estimate scale parameter for multiresolution image segmentation of remotely sensed data. *Int. J. Geographical Information Science* 24 (6), 859–871.
- Du, P., Samat, A., Waske, B., Liu, S., Li, Z., 2015. Random forest and rotation forest for fully polarized SAR image classification using polarimetric and spatial features. *ISPRS J. Photogramm. Remote Sens.* 105, 38–53.
- Embersson, R., Kirschbaum, D., Stanley, T., 2021. Global connections between El Niño and landslide impacts. *Nat. Commun.* 12, 1–11.
- Falco, N., Marpu, P.R., Benediktsson, J.A., 2016. A toolbox for unsupervised change detection analysis. *Int. J. Remote Sens.* 37 (7), 1505–1526.
- Fan, X., Scaringi, G., Xu, Q., Zhan, W., Dai, L., Li, Y., Pei, X., Yang, Q., Huang, R., 2018. Co-seismic landslides triggered by the 8th August 2017 M_s 7.0 Jiuzhaigou earthquake (Sichuan, China): factors controlling their spatial distribution and implications for the seismogenic blind fault identification. *Landslides* 15, 967–983.
- Fauvel, M., Benediktsson, J.A., Chanussot, J., Sveinsson, J.R., 2008. Spectral and spatial classification of hyperspectral data using SVMs and morphological profiles. *IEEE Trans. Geosci. Remote Sens.* 46 (11), 3804–3814.
- Fiorucci, F., Ardizzone, F., Mondini, A.C., Viero, A., Guzzetti, F., 2019. Visual interpretation of stereoscopic NVDI satellite images to map rainfall-induced landslides. *Landslides* 16 (1), 165–174.
- Fiorucci, F., Cardinali, M., Carli, R., Rossi, M., Mondini, A.C., Santurri, L., Ardizzone, F., Guzzetti, F., 2011. Seasonal landslide mapping and estimation of landslide mobilization rates using aerial and satellite images. *Geomorphology* 129 (1–2), 59–70.
- Galli, M., Ardizzone, F., Cardinali, M., Guzzetti, F., Reichenbach, P., 2008. Comparing landslide inventory maps. *Geomorphology* 94 (3–4), 268–289.
- Gao, J., Maro, J., 2010. Topographic controls on evolution of shallow landslides in pastoral Wairarapa, New Zealand, 1979–2003. *Geomorphology* 114 (3), 373–381.
- Gorum, T., Fan, X., van Westen, C.J., Huang, R.Q., Xu, Q., Tang, C., Wang, G., 2011. Distribution pattern of earthquake-induced landslides triggered by the 12 May 2008 Wenchuan earthquake. *Geomorphology* 133 (3–4), 152–167.
- Gu, Y., Liu, T., Jia, X., Benediktsson, J.A., Chanussot, J., 2016. Nonlinear multiple kernel learning with multiple-structure-element extended morphological profiles for hyperspectral image classification. *IEEE Trans. Geosci. Remote Sens.* 54 (6), 3235–3247.
- Guzzetti, F., Mondini, A.C., Cardinali, M., Fiorucci, F., Santangelo, M., Chang, K.-T., 2012. Landslide inventory maps: New tools for an old problem. *Earth Sci. Rev.* 112 (1–2), 42–66.
- Höbling, D., Friedl, B., Eisank, C., 2015. An object-based approach for semi-automated landslide change detection and attribution of changes to landslide classes in northern Taiwan. *Earth Sci. Inf.* 8 (2), 327–335.
- Hossain, M.D., Chen, D., 2019. Segmentation for Object-Based Image Analysis (OBIA): A review of algorithms and challenges from remote sensing perspective. *ISPRS J. Photogramm. Remote Sens.* 150, 115–134.
- Hou, Z., Li, W., Li, L., Tao, R., Du, Q., 2022. Hyperspectral Change Detection Based on Multiple Morphological Profiles. *IEEE Trans. Geosci. Remote Sens.* 60, 1–12.
- Hu, K., Zhang, X., You, Y., Hu, X., Liu, W., Li, Y., 2019. Landslides and dammed lakes triggered by the 2017 Ms6.9 Milin earthquake in the Tsangpo gorge. *Landslides* 16, 993–1001.
- Hu, X., An, W., Garzanti, E., Liu, Q., 2020. Recognition of trench basins in collisional orogens: Insights from the Yarlung Zangbo suture zone in southern Tibet. *Science China Earth Sciences* 63 (12), 2017–2028.
- Hu, Z., Shi, T., Wang, C., Li, Q., Wu, G., 2021. Scale-sets image classification with hierarchical sample enriching and automatic scale selection. *Int. J. Appl. Earth Obs. Geoinf.* 105, 102605. <https://doi.org/10.1016/j.jag.2021.102605>.

- Huang, R., Fan, X., 2013. The landslide story. *Nat. Geosci.* 6 (5), 325–326.
- Huang, R., Pei, X., Fan, X., Zhang, W., Li, S., Li, B., 2012. The characteristics and failure mechanism of the largest landslide triggered by the Wenchuan earthquake, May 12, 2008, China. *Landslides* 9 (1), 131–142.
- Huang, X., Han, X., Zhang, L., Gong, J., Liao, W., Benediktsson, J.A., 2016. Generalized differential morphological profiles for remote sensing image classification. *IEEE J. Sel. Top. Appl. Earth Obs. Remote Sens.* 9 (4), 1736–1751.
- Hussain, M., Chen, D., Cheng, A., Wei, H., Stanley, D., 2013. Change detection from remotely sensed images: From pixel-based to object-based approaches. *ISPRS J. Photogramm. Remote Sens.* 80, 91–106.
- Iwahashi, J., Kamiya, I., Yamagishi, H., 2012. High-resolution DEMs in the study of rainfall-and earthquake-induced landslides: Use of a variable window size method in digital terrain analysis. *Geomorphology* 153–154, 29–38.
- Johnson, B., Xie, Z., 2011. Unsupervised image segmentation evaluation and refinement using a multi-scale approach. *ISPRS J. Photogramm. Remote Sens.* 66 (4), 473–483.
- Kritikos, T., Robinson, T.R., Davies, T.R.H., 2015. Regional coseismic landslide hazard assessment without historical landslide inventories: A new approach. *J. Geophys. Res. Earth Surf.* 120 (4), 711–729.
- Lagrange, A., Fauvel, M., Grizonnet, M., 2017. Large-scale feature selection with Gaussian mixture models for the classification of high dimensional remote sensing images. *IEEE Trans. Comput. Imaging* 3 (2), 230–242.
- Lei, T., Zhang, Y., Lv, Z., Li, S., Liu, S., Nandi, A.K., 2019. Landslide inventory mapping from bitemporal images using deep convolutional neural networks. *IEEE Geosci. Remote Sens. Lett.* 16 (6), 982–986.
- Li, Z., Shi, W., Lu, P., Yan, L., Wang, Q., Miao, Z., 2016. Landslide mapping from aerial photographs using change detection-based Markov random field. *Remote Sens. Environ.* 187, 76–90.
- Licciardi, G., Marpu, P.R., Chanussot, J., Benediktsson, J.A., 2012. Linear versus nonlinear PCA for the classification of hyperspectral data based on the extended morphological profiles. *IEEE Geosci. Remote Sens. Lett.* 9 (3), 447–451.
- Lin, C.-W., Shieh, C.-L., Yuan, B.-D., Shieh, Y.-C., Liu, S.-H., Lee, S.-Y., 2004. Impact of Chi-Chi earthquake on the occurrence of landslides and debris flows: example from the Chenyulan River watershed, Nantou, Taiwan. *Engineering Geology* 71 (1–2), 49–61.
- Liu, S., Du, Q., Tong, X., Samat, A., Bruzzone, L., Bovolo, F., 2017. Multiscale morphological compressed change vector analysis for unsupervised multiple change detection. *IEEE J. Sel. Top. Appl. Earth Obs. Remote Sens.* 10 (9), 4124–4137.
- Lu, P., Qin, Y., Li, Z., Mondini, A.C., Casagli, N., 2019. Landslide mapping from multi-sensor data through improved change detection-based Markov random field. *Remote Sens. Environ.* 231, 111235. <https://doi.org/10.1016/j.rse.2019.111235>.
- Lu, P., Shi, W., Wang, Q., Li, Z., Qin, Y., Fan, X., 2021. Co-seismic landslide mapping using Sentinel-2 10-m fused NIR narrow, red-edge, and SWIR bands. *Landslides* 18 (6), 2017–2037.
- Lu, P., Stumpf, A., Kerle, N., Casagli, N., 2011. Object-oriented change detection for landslides rapid mapping. *IEEE Geosci. Remote Sens. Lett.* 8 (4), 701–705.
- Malamud, B.D., Turcotte, D.L., Guzzetti, F., Reichenbach, P., 2004. Landslides, earthquakes, and erosion. *Earth Planet. Sci. Lett.* 229 (1–2), 45–59.
- Martha, T.R., Kerle, N., van Westen, C.J., Jetten, V., Kumar, K.V., 2011. Segment optimization and data-driven thresholding for knowledge-based landslide detection by object-based image analysis. *IEEE Trans. Geosci. Remote Sens.* 49 (12), 4928–4943.
- Martha, T.R., Kerle, N., van Westen, C.J., Jetten, V., Vinod Kumar, K., 2012. Object-oriented analysis of multi-temporal panchromatic images for creation of historical landslide inventories. *ISPRS J. Photogramm. Remote Sens.* 67, 105–119.
- Martinez, S.N., Allstadt, K.E., Slaughter, S.L., Schmitt, R.G., Collins, E., Schaefer, L.N., & Ellison, S. (2021). Landslides triggered by the August 14, 2021, magnitude 7.2 Nippes, Haiti, earthquake. In: US Geological Survey. <https://doi.org/10.3133/ofr20211112>.
- Maulik, U., Chakraborty, D., 2017. Remote Sensing Image Classification: A survey of support-vector-machine-based advanced techniques. *IEEE Geosci. Remote Sens. Mag.* 5 (1), 33–52.
- Melgani, F., Bazi, Y., 2008. Classification of electrocardiogram signals with support vector machines and particle swarm optimization. *IEEE Trans. Inf. Technol. Biomed.* 12 (5), 667–677.
- Metternicht, G., Hurni, L., Gogu, R., 2005. Remote sensing of landslides: An analysis of the potential contribution to geo-spatial systems for hazard assessment in mountainous environments. *Remote Sens. Environ.* 98 (2–3), 284–303.
- Ming, D., Li, J., Wang, J., Zhang, M., 2015. Scale parameter selection by spatial statistics for GeoBIA: Using mean-shift based multi-scale segmentation as an example. *ISPRS J. Photogramm. Remote Sens.* 106, 28–41.
- Mongus, D., Lukač, N., Žalik, B., 2014. Ground and building extraction from LiDAR data based on differential morphological profiles and locally fitted surfaces. *ISPRS J. Photogramm. Remote Sens.* 93, 145–156.
- Moosavi, V., Talebi, A., Shirmohammadi, B., 2014. Producing a landslide inventory map using pixel-based and object-oriented approaches optimized by Taguchi method. *Geomorphology* 204, 646–656.
- Mountrakis, G., Im, J., Ogole, C., 2011. Support vector machines in remote sensing: A review. *ISPRS J. Photogramm. Remote Sens.* 66 (3), 247–259.
- Niu, C., Zhang, H., Liu, W., Li, R., Hu, T., 2021. Using a fully polarimetric SAR to detect landslide in complex surroundings: Case study of 2015 Shenzhen landslide. *ISPRS J. Photogramm. Remote Sens.* 174, 56–67.
- Okay, U., Telling, J., Glennie, C.L., Dietrich, W.E., 2019. Airborne lidar change detection: An overview of Earth sciences applications. *Earth Sci. Rev.* 198, 102929. <https://doi.org/10.1016/j.earscirev.2019.102929>.
- Otsu, N., 1979. A threshold selection method from gray-level histograms. *IEEE Transactions on Systems, Man, and Cybernetics* 9 (1), 62–66.
- Panuntun, H., 2021. The 2021 Mw 7.2 Haiti Earthquake: Rupture of a Blind Thrust Fault Revealed by Space Geodetic Observations. *Earth and Space Science Open Archive* 16. <https://doi.org/10.1002/essoar.10508758.1>.
- Reichenbach, P., Rossi, M., Malamud, B.D., Mihir, M., Guzzetti, F., 2018. A review of statistically-based landslide susceptibility models. *Earth Sci. Rev.* 180, 60–91.
- Rodriguez-Galiano, V.F., Ghimire, B., Rogan, J., Chica-Olmo, M., Rigol-Sanchez, J.P., 2012. An assessment of the effectiveness of a random forest classifier for land-cover classification. *ISPRS J. Photogramm. Remote Sens.* 67, 93–104.
- Rodriguez, J.J., Kuncheva, L.I., Alonso, C.J., 2006. Rotation forest: A new classifier ensemble method. *IEEE Trans. Pattern Anal. Mach. Intell.* 28 (10), 1619–1630.
- Scheip, C.M., Wegmann, K.W., 2021. HazMapper: A global open-source natural hazard mapping application in Google Earth Engine. *Nat. Hazards Earth Syst. Sci.* 21 (5), 1495–1511.
- Schulz, W.H., Kean, J.W., Wang, G., 2009. Landslide movement in southwest Colorado triggered by atmospheric tides. *Nat. Geosci.* 2 (12), 863–866.
- Shen, D., Shi, Z., Peng, M., Zhang, L., Zhu, Y., 2021. Preliminary analysis of a rainfall-induced landslide hazard chain in Enshi City, Hubei Province, China in July 2020. *Landslides* 18 (1), 509–512.
- Shen, H., Lin, Y., Tian, Q., Xu, K., Jiao, J., 2018. A comparison of multiple classifier combinations using different voting-weights for remote sensing image classification. *Int. J. Remote Sens.* 39 (11), 3705–3722.
- Sheykhou, M., Mahdianpari, M., Ghanbari, H., Mohammadimanesh, F., Ghamisi, P., & Homayouni, S. (2020). Support vector machine vs. random forest for remote sensing image classification: A meta-analysis and systematic review. *IEEE Journal of Selected Topics in Applied Earth Observations and Remote Sensing*.
- Shi, W., Zhang, M., Ke, H., Fang, X., Zhan, Z., Chen, S., 2021. Landslide recognition by deep convolutional neural network and change detection. *IEEE Trans. Geosci. Remote Sens.* 59 (6), 4654–4672.
- Soille, P., 2013. Morphological image analysis: principles and applications. Springer Science & Business Media. <https://doi.org/10.1007/978-3-662-03939-7>.
- Valagussa, A., Marc, O., Frattini, P., Crosta, G.B., 2019. Seismic and geological controls on earthquake-induced landslide size. *Earth Planet. Sci. Lett.* 506, 268–281.
- Valero, S., Chanussot, J., Benediktsson, J.A., Talbot, H., Waske, B., 2010. Advanced directional mathematical morphology for the detection of the road network in very high resolution remote sensing images. *Pattern Recogn. Lett.* 31 (10), 1120–1127.
- Valkaniotis, S., Papathanassiou, G., Ganas, A., 2018. Mapping an earthquake-induced landslide based on UAV imagery: case study of the 2015 Okeanos landslide, Lefkada, Greece. *Eng. Geol.* 245, 141–152.
- Volpi, M., Tuia, D., Bovolo, F., Kanevski, M., Bruzzone, L., 2013. Supervised change detection in VHR images using contextual information and support vector machines. *Int. J. Appl. Earth Obs. Geoinf.* 20, 77–85.
- Walter, V., 2004. Object-based classification of remote sensing data for change detection. *ISPRS J. Photogramm. Remote Sens.* 58, 225–238.
- Wang, X., Du, P., Chen, D., Lin, C., Zheng, H., Guo, S., 2020. Characterizing urbanization-induced land surface phenology change from time-series remotely sensed images at fine spatio-temporal scale: A case study in Nanjing, China (2001–2018). *J. Cleaner Prod.* 274, 122487. <https://doi.org/10.1016/j.jclepro.2020.122487>.
- Wang, Y., Qi, Q., Liu, Y., Jiang, L., Wang, J., 2019. Unsupervised segmentation parameter selection using the local spatial statistics for remote sensing image segmentation. *Int. J. Appl. Earth Obs. Geoinf.* 81, 98–109.
- Wang, Y., Tian, Z., Qi, Q., Wang, J., 2021. Double-Variance Measures: A Potential Approach to Parameter Optimization of Remote Sensing Image Segmentation. *IEEE J. Sel. Top. Appl. Earth Obs. Remote Sens.* 14, 2314–2326.
- Wozniak, M., Grana, M., Corchado, E., 2014. A survey of multiple classifier systems as hybrid systems. *Information Fusion* 16, 3–17.
- Xia, J., Du, P., He, X., Chanussot, J., 2013. Hyperspectral remote sensing image classification based on rotation forest. *IEEE Geosci. Remote Sens. Lett.* 11, 239–243.
- Yang, W., Qi, W., Fang, J., 2020. Using Google Earth Engine to monitor co-seismic landslide recovery after the 2008 Wenchuan earthquake. *Earth Surf. Dyn. Discuss.* <https://doi.org/10.5194/esurf-2020-106>.
- Zhang, J., Westen, C.J.v., Tanyas, H., Mavrouli, O., Ge, Y., Bajrachary, S., Gurung, D.R., Dhital, M.R., & Khanal, N.R. (2019). How size and trigger matter: analyzing rainfall-and earthquake-triggered landslide inventories and their causal relation in the Koshi River basin, central Himalaya. *Natural Hazards and Earth System Sciences*, 19, 1789–1805.
- Zhang, W., Lu, X., Li, X., 2018. A coarse-to-fine semi-supervised change detection for multispectral images. *IEEE Trans. Geosci. Remote Sens.* 56, 3587–3599.
- Zhang, X., Xiao, P., Feng, X., 2020. Object-specific optimization of hierarchical multiscale segmentations for high-spatial resolution remote sensing images. *ISPRS J. Photogramm. Remote Sens.* 159, 308–321.
- Zhao, B., Li, W., Wang, Y., Lu, J., Li, X., 2019. Landslides triggered by the Ms 6.9 Nyingchi earthquake, China (18 November 2017): analysis of the spatial distribution and occurrence factors. *Landslides* 16, 765–776.
- Zhao, M., Li, L., Li, W., Tao, R., Li, L., Zhang, W., 2020. Infrared small-target detection based on multiple morphological profiles. *IEEE Trans. Geosci. Remote Sens.*
- Zhong, C., Liu, Y., Gao, P., Chen, W., Li, H., Hou, Y., Nuremagul, T., Ma, H., 2020. Landslide mapping with remote sensing: challenges and opportunities. *Int. J. Remote Sens.* 41, 1555–1581.